Research Square

Preprints are preliminary reports that have not undergone peer review.
They should not be considered conclusive, used to inform clinical practice,
or referenced by the media as validated information.

Bioactive Metal-Phenolic Network and Prebiotic Hydrogel Synergize with Mesenchymal stem cell-derived extracellular vesicles for Microenvironment-Modulating Therapy of Inflammatory Bowel Disease

Qi Pan
Northwestern Polytechnical University
Pei Li
Northwestern Polytechnical University
Yingfeng Gao
Northwestern Polytechnical University
Na Zhao
Northwestern Polytechnical University
Miao Yu
Northwestern Polytechnical University
Zhongxue Wang
Northwestern Polytechnical University
Xuanqi Feng
Chinese University of Hong Kong, Shenzhen
Chenghu Hu
chenghu@nwpu.edu.cn
Northwestern Polytechnical University
Zhang Yuan
Northwestern Polytechnical University
Chengbiao Hu
Northwestern Polytechnical University

Research Article

Keywords: Extracellular vesicles, Mesenchymal stem cells, Oral drug delivery, Inflammatory bowel disease, Metal-polyphenol networks, Immunomodulation, Gut microbiota remodeling, Nanotheraeutics

Posted Date: August 10th, 2026

DOI: https://doi.org/10.21203/rs.3.rs-10544945/v1

License: This work is licensed under a Creative Commons Attribution 4.0 International License.
Read Full License

Additional Declarations: No competing interests reported.

Bioactive Metal-Phenolic Network and Prebiotic Hydrogel Synergize with Mesenchymal stem cell-derived extracellular vesicles for Microenvironment-Modulating Therapy of Inflammatory Bowel Disease

Qi Pan1†, Pei Li1†, Yingfeng Gao1,2†, Na Zhao1, Miao Yu1, Zhongxue Wang1, Xuanqi Feng3, Chenghu Hu1,2*, Zhang Yuan1* and Chengbiao Hu1*

1 Xi'an Key Laboratory of Stem Cell and Regenerative Medicine, School of Life Science and Technology, Northwestern Polytechnical University, 127 West Youyi Road, Beilin District, Xi'an, Shaanxi 710072, P. R. China

2 State Key Laboratory of Southwestern Chinese Medicine Resources, Hospital of Chengdu University of Traditional Chinese Medicine, School of Pharmacy, Chengdu University of Traditional Chinese Medicine, Chengdu 611137, P. R. China

3 School of Medicine, The Chinese University of Hong Kong, Shenzhen, Guangdong, 518172, P.R. China

*Corresponding authors.

*E-mail addresses:

chenghu@nwpu.edu.cn (Chenghu Hu)，yuanzhang1993@nwpu.edu.cn (Zhang yuan), hcbhappy@nwpu.edu.cn (Chengbiao Hu).

†These authors made equal contributions to this work.

Abstract

Mesenchymal stem cell-derived extracellular vesicles (MVs) holds great promise for inflammatory bowel disease (IBD) therapy. However, oral delivery of MVs therapeutic efficacy is severely compromised by the harsh gastrointestinal environment and the hostile inflammatory milieu, characterized by excessive oxidative stress and dysbiosis. To surmount these biological barriers, we engineered Inu@MPN@MV, a multifunctional oral delivery platform that integrates MVs with a

caffeic acid-Fe^{3+} metal-phenolic network (MPN) coating and an inulin-based hydrogel matrix. In this synergistic system, the inulin hydrogel provides gastric protection and enables colon-specific release, while simultaneously functioning as a prebiotic to foster a beneficial microbial niche. Concurrently, the MPN coating endows the vesicles with potent ROS-scavenging capabilities, shielding them from oxidative damage and promoting their accumulation at inflamed sites. In a dextran sulfate sodium (DSS)-induced colitis model, oral administration of Inu@MPN@MV yielded superior therapeutic outcomes compared to controls, effectively ameliorating clinical symptoms, restoring epithelial barrier integrity, and mitigating oxidative injury. Mechanistically, the formulation orchestrates a synergistic interplay between the immunoregulatory cargo of MVs and the microenvironment-modulating properties of the carrier. This combination reprograms macrophage polarization toward an anti-inflammatory phenotype, remodels gut microbiota composition, and restores metabolic homeostasis. Collectively, this study presents a rationally designed bioactive oral system where carrier components actively potentiate the intrinsic therapeutic effects of MVs, offering a robust strategy for IBD management.

KEYWORDS

Extracellular vesicles, Mesenchymal stem cells, Oral drug delivery, Inflammatory bowel disease, Metal-polyphenol networks, Immunomodulation, Gut microbiota remodeling, Nanotheraeutics

Introduction

Inflammatory bowel disease (IBD), mainly comprising ulcerative colitis and Crohn's disease, is a chronic and relapsing inflammatory disorder of the gastrointestinal tract [1–3]. Although biologics, small-molecule inhibitors, immunosuppressants, and other anti-inflammatory agents have expanded current treatment options, many patients still fail to achieve durable remission or gradually lose response during long-term therapy [1,2,4]. This limited therapeutic durability reflects the multifactorial and self-reinforcing nature of IBD [3,5,6]. Intestinal inflammation is maintained not by a single immune pathway, but by reciprocal disruption of mucosal immune homeostasis, epithelial barrier integrity, redox balance, and the gut microbial ecosystem [3,5,7,8]. In the inflamed colon, excessive cytokine signaling activates mucosal immune cells and aggravates epithelial injury, while reactive oxygen species (ROS) damage tight-junction structures, promote lipid peroxidation, and increase mucosal permeability[4,5,9]. Meanwhile, dysbiosis and altered microbial metabolites weaken epithelial repair, disturb mucosal immune tolerance, and reduce intestinal ecological resilience [6–8,10]. These events establish a vicious cycle of inflammation, oxidative injury, barrier dysfunction, and microbial imbalance [3,5,7,8]. Therefore, effective local treatment should not only suppress inflammatory signaling, but also provide conditions that permit sustained immune regulation and epithelial recovery [4,5,10].

Mesenchymal stem cell (MSC)-based therapy has shown considerable potential in IBD because MSCs can suppress inflammatory cytokine production, regulate macrophage and T-cell responses, and promote epithelial regeneration [11,12].

Increasing evidence indicates, however, that many of these effects are mediated predominantly by paracrine factors rather than by long-term engraftment of transplanted cells [11,12]. Among the principal paracrine effectors, MSC-derived extracellular vesicles (MVs), including exosomes and microvesicles, have attracted particular attention [13–15]. These membrane-bound nanoparticles transport proteins, lipids, and nucleic acids inherited from their parent cells and deliver bioactive cargos to recipient cells, thereby reproducing many immunomodulatory and regenerative functions of MSCs [13–16]. Compared with living-cell products, MVs are easier to store, standardize, and engineer, and may reduce concerns associated with poor cell survival, ectopic differentiation, vascular embolism, and batch-to-batch variability [11,15–17]. In experimental colitis, MVs alleviate intestinal inflammation by regulating macrophage polarization, suppressing inflammatory cytokine production, and accelerating epithelial repair [11,12,18]. These properties identify MVs as attractive cell-free effectors for IBD therapy [11,12,16]. Their therapeutic value, however, depends on reaching the diseased intestine in an intact and biologically active state [16–19].

Most studies of MVs in colitis still rely on injection-based administration [11,12]. Although systemic delivery is useful for proof-of-concept studies, it is not ideally matched to a chronic disease primarily located in the gastrointestinal tract [19,20]. Repeated injections reduce patient convenience and may expose MVs to broad systemic distribution before sufficient amounts reach the inflamed colon [19,20]. Oral administration is therefore attractive because it is non-invasive, patient-friendly, and

anatomically aligned with local intestinal treatment [21–23]. Nevertheless, mammalian vesicles are vulnerable to the harsh gastrointestinal environment [23,24]. Gastric acid, digestive enzymes, bile salts, and mechanical stress can disrupt the vesicular lipid membrane and damage bioactive cargos, making it difficult for unprotected MVs to arrive at the colon in sufficient quantities [21–24]. This challenge has prompted the development of protective oral MV formulations [21–23]. Gan et al. encapsulated MSC-derived exosomes in oral microcapsules for acute colitis treatment, demonstrating that a protective matrix can improve vesicle survival during gastrointestinal transit and permit therapeutic activity after oral administration [21]. Deng et al. further developed layer-by-layer coated exosomes to enhance vesicle stability and promote colonic delivery through the oral route [22]. These studies established the feasibility of oral MV therapy [21–23]. However, existing strategies have focused mainly on protection during transit and delivery efficiency, while paying less attention to MV performance after release into an inflamed colon characterized by excessive ROS, damaged epithelium, activated immune cells, and disrupted microbial metabolism [9,10,25,26].

This post-release challenge is especially relevant for MV therapy [9,10,25,26]. MVs are intended to regulate inflammatory cells and promote tissue repair, but their effects must occur within a pathological environment that can continuously reactivate immune signaling and injure recipient cells [5,9,25,26]. Persistent ROS accumulation impairs mitochondrial function, weakens endogenous antioxidant defenses, and aggravates epithelial and macrophage dysfunction [9,25,26]. Microbial dysbiosis and

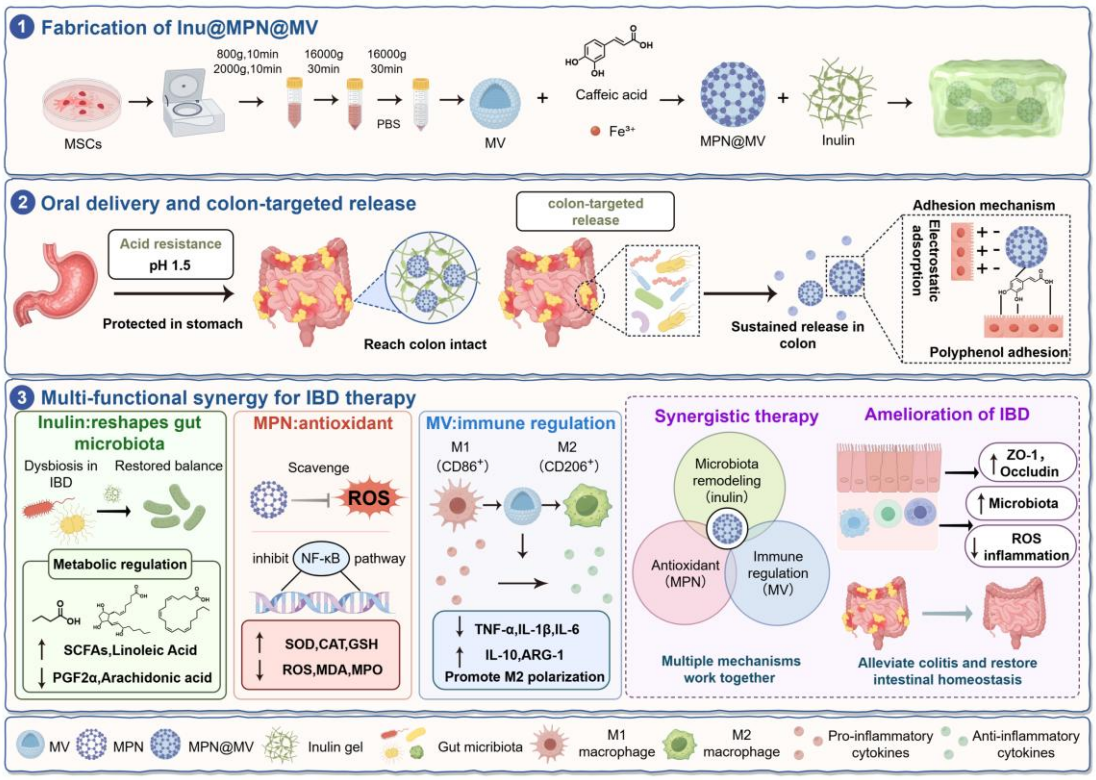
abnormal metabolites can also maintain mucosal immune activation after part of the inflammatory signaling has been suppressed [6,7,10,27]. Thus, a rational oral MV formulation should satisfy two sequential requirements: preserving MVs during gastrointestinal transit and providing a more permissive local environment for MV-mediated immunoregulation after colonic release [22,23,25,28]. Therefore, Supporting materials should protect MV integrity, improve local retention, and reduce environmental constraints on their biological performance [22,23,25,28].

Inulin provides a suitable matrix for this purpose [29–32]. As a prebiotic fructan, inulin resists digestion in the upper gastrointestinal tract and can be fermented by colonic microbiota, supporting its use in colon-oriented delivery and intestinal ecological regulation [29,30]. When formulated as a hydrogel, inulin can physically shield MV from gastric degradation, prolong gastrointestinal residence, and enable distal intestinal release [31–33]. Its fermentability may also support beneficial microbial populations and microbial metabolic functions during mucosal recovery [27,29,30]. By improving gastric protection, colonic release, and local residence, the hydrogel increases the likelihood that biologically active MVs will reach diseased intestinal sites [31–33]. Its prebiotic property provides an additional supportive context [29,30].To further support MV function after colonic release, metal–phenolic network (MPN) surface engineering offers a complementary strategy [34,35]. MPNs are formed through coordination between metal ions and phenolic ligands and can be assembled under mild aqueous conditions, allowing biological nanoparticles to be functionalized without harsh processing [34,35]. Here, caffeic acid and Fe^{3+} were used

to construct a thin MPN layer on MVs. The catechol groups of caffeic acid coordinate with Fe^{3+} and provide redox-active phenolic motifs, thereby introducing ROS-scavenging capacity around the MV surface [34,35]. This feature is relevant because the inflamed colon is characterized by excessive ROS accumulation, impaired antioxidant defense, mitochondrial dysfunction, and oxidative damage to epithelial and immune cells [9,25,26]. Reducing the local oxidative burden may preserve recipient-cell responsiveness and provide a more favorable context for MV-mediated immune regulation [9,25]. In addition, phenolic hydroxyl- and catechol-rich surfaces can participate in multivalent hydrogen-bonding and coordination interactions with mucin- and protein-rich interfaces, while electrostatic interactions with exposed inflammatory components may support retention at injured sites [28,35].

Based on these considerations, we developed Inu@MPN@MV as an oral MV-centered delivery system for IBD therapy (Scheme 1). MVs serve as the principal biological effectors responsible for immunomodulation and tissue repair. The caffeic acid–Fe^{3+} MPN shell buffers excessive oxidative stress and supports local enrichment, whereas the inulin hydrogel protects the formulation during gastrointestinal transit, enables colon-oriented release, prolongs intestinal exposure, and provides a supportive prebiotic matrix. Unlike previous oral MV systems that primarily address gastrointestinal stability, this design seeks to preserve MV activity both before arrival in the colon and after release into the diseased microenvironment. We evaluated the formulation in a dextran sulfate sodium-induced colitis model and examined

macrophage activation, oxidative injury, epithelial barrier integrity, gut microbial composition, fecal metabolism, and host transcriptional responses. Oral Inu@MPN@MV alleviated disease severity, restored barrier-associated structures, reduced inflammatory and oxidative injury, promoted reparative macrophage polarization, and shifted microbial, metabolic, and transcriptional profiles toward intestinal homeostasis. These findings support a microenvironment-supportive oral delivery strategy that enables MVs to function more effectively in the inflamed intestine.



Scheme 1. Schematic diagram illustrating the multi-functional synergistic regulatory mechanism of Inu@MPN@MV in the treatment of IBD. Inu@MPN@MV is designed to protect MV during gastrointestinal transit, enable colonic release and retention,

scavenge reactive oxygen species, modulate gut microbiota, regulate macrophage polarization, and promote epithelial barrier repair in DSS-induced colitis.

Methods

Materials

Inulin from chicory, caffeic acid, and iron(III) chloride hexahydrate (FeCl3·6H2O) were purchased from Aladdin (China). PKH26, DAPI, DCFH-DA, JC-1, CCK-8, and biochemical assay kits for malondialdehyde (MDA), myeloperoxidase (MPO), superoxide dismutase (SOD), catalase (CAT), glutathione (GSH), and ATP were purchased from Beyotime (China). DSS (36,000–50,000 Da) was purchased from MP Biomedicals. All other chemicals were acquired from Sigma-Aldrich (St. Louis, MO, USA) and Shanghai Chemical Reagents Co. (China) and used as received unless otherwise specified.

Isolation and culture of hUC-MSCs and collection of MSC-derived extracellular vesicles

Human umbilical cord mesenchymal stem cells (hUC-MSCs) were cultured in Dulbecco's modified Eagle's medium/F12 (DMEM/F12) supplemented with 10% fetal bovine serum (FBS) and 1% penicillin-streptomycin in a humidified incubator at 37 °C with 5% CO_2. Cells between passages 4 and 7 were used for all experiments. When the cells reached approximately 80–90% confluence, they were washed twice with phosphate-buffered saline (PBS) and cultured in serum-free DMEM/F12 for an

additional 48 h.The conditioned medium was collected and sequentially centrifuged at 800 × g for 10 min and 2,000 × g for 10 min at 4 °C to remove intact cells and cellular debris. MVs were subsequently pelleted by centrifugation at 16,000 × g for 30 min at 4 °C. The collected MVs were washed three times with sterile PBS using the same centrifugation conditions and resuspended in PBS. The suspension was passed through a 0.22 μm syringe filter to remove residual impurities. The protein concentration of purified MVs was determined using a bicinchoninic acid (BCA) protein assay. Purified MVs were either used immediately or stored at −80 °C until further use.

Preparation of MPN-coated MVs

MPN-coated MVs (MPN@MV) were prepared through the coordination-driven self-assembly of caffeic acid (CA) and Fe^{3+} on the surface of MVs. Briefly, caffeic acid was dissolved in ultrapure water and adjusted to pH 7.4, while $FeCl_3 \cdot 6H_2O$ was freshly dissolved in ultrapure water immediately before use. The MV suspension was mixed with CA and $FeCl_3 \cdot 6H_2O$ at a mass ratio of MV:CA:Fe^{3+} = 10:4:1. The mixture was vortexed for 2 min at room temperature, and the vortexing process was repeated three times to allow the coordination assembly of the metal-phenolic network on the MV surface. The suspension was centrifuged at 4,000 × g for 3 min at 4 °C to remove unbound metal-phenolic precipitates, and the supernatant containing MPN@MV was collected for subsequent experiments.

Preparation of Inu@MPN@MV hydrogel

Inu@MPN@MV hydrogel was prepared by thermal gelation of inulin. Briefly, 0.4 g of inulin was dissolved in 1 mL of ultrapure water under magnetic stirring at 85 °C for 10 min until a homogeneous solution was obtained. The solution was then allowed to cool naturally to room temperature, followed by the addition of the MPN@MV suspension to achieve a final MV protein concentration of 0.8 mg/mL. The mixture was further stirred for 10 min at room temperature and subsequently incubated at 4 °C overnight to allow complete gelation. Blank inulin hydrogel and Inu@MV hydrogel were prepared using the same procedure by replacing MPN@MV with PBS and unmodified MVs, respectively.

Physicochemical characterization

The hydrodynamic diameter, polydispersity index (PDI), and zeta potential of MVs and MPN@MV were measured by dynamic light scattering (DLS) using a NanoBrook 90Plus Zeta analyzer (Brookhaven Instruments, USA).The morphology of MVs, MPN@MV, and MVs released from Inu@MPN@MV was characterized by transmission electron microscopy (TEM) after negative staining with 2% phosphotungstic acid for 3 min. The successful formation of the metal-phenolic coating was further evaluated by ultraviolet-visible (UV–vis) spectroscopy, X-ray photoelectron spectroscopy (XPS), and elemental mapping.The microstructure of freeze-dried inulin hydrogels was observed by scanning electron microscopy (SEM). Briefly, hydrogel samples were frozen in liquid nitrogen, freeze-dried, fractured, sputter-coated with gold, and then imaged by SEM. The rheological properties of the

hydrogels were evaluated using frequency sweep and time sweep measurements to investigate their viscoelastic behavior and gelation properties.

In vitro antioxidant activity, stability, and release

The free radical-scavenging activity of MPN@MV was evaluated using commercial ABTS and DPPH radical scavenging assay kits (Beyotime, China) according to the manufacturer's instructions.To evaluate the degradation behavior of the hydrogel, Inu@MPN@MV hydrogel was incubated in phosphate-buffered saline (PBS) at pH 1.5, 6.0, 7.4, or 8.0 at 37 °C with shaking at 200 rpm. At predetermined time points, the residual hydrogel was collected, gently blotted with filter paper to remove excess buffer, and weighed. The remaining hydrogel mass was calculated relative to the initial weight.For the *in vitro* release study, Inu@MPN@MV hydrogel was incubated in PBS (pH 8.0) at 37 °C with gentle shaking. At predetermined time intervals, the supernatant was collected after centrifugation and replaced with an equal volume of fresh PBS. The amount of released MVs was quantified using a bicinchoninic acid (BCA) protein assay. The morphology and particle size of the released MVs were further characterized by TEM and DLS, respectively, as described above.

Cell culture

RAW264.7 macrophages were cultured in Dulbecco's modified Eagle's medium (DMEM) supplemented with 10% fetal bovine serum (FBS) and 1% penicillin-streptomycin at 37 °C in a humidified incubator containing 5% CO_2.

Cytocompatibility Assay

RAW264.7 macrophages were seeded into 96-well plates and allowed to adhere overnight. Cells were then incubated with MVs or MPN@MV at different MV protein concentrations (12.5, 25, 50, and 100 μg/mL) for 24 h. Cell viability was evaluated using a Cell Counting Kit-8 (CCK-8, Beyotime, China) according to the manufacturer's instructions. The absorbance at 450 nm was measured using a microplate reader, and cell viability was expressed relative to untreated cells.

Cellular uptake

MVs and MPN@MV were labeled with PKH26 (Beyotime, China) according to the manufacturer's instructions. RAW264.7 macrophages were seeded onto confocal dishes and cultured overnight before incubation with PKH26-labeled MVs or MPN@MV for 3 h. The cells were subsequently washed three times with PBS, fixed with 4% paraformaldehyde for 15 min, stained with DAPI, and observed using a confocal laser scanning microscope (CLSM).

Macrophage polarization by immunofluorescence

RAW264.7 macrophages were seeded onto confocal dishes and cultured overnight. Cells were simultaneously treated with lipopolysaccharide (LPS, 1 μg/mL) and different formulations for 24 h. After treatment, the cells were washed with PBS, fixed with 4% paraformaldehyde for 15 min, permeabilized with 0.2% Triton X-100, and blocked with 5% bovine serum albumin (BSA). The cells were then incubated with primary antibodies against CD86 or CD206 overnight at 4 °C, followed by incubation with the corresponding fluorescent secondary antibodies for 1 h at room temperature. Cell nuclei were counterstained with DAPI, and fluorescence images were acquired using a confocal laser scanning microscope (CLSM).

Quantitative Real-Time PCR assay

RAW264.7 macrophages were simultaneously treated with LPS (1 μg/mL) and different formulations for 24 h. Total RNA was extracted using a commercial RNA extraction kit according to the manufacturer's instructions. Complementary DNA (cDNA) was synthesized by reverse transcription, and quantitative real-time PCR (qRT-PCR) was performed using a SYBR Green Master Mix. Relative gene expression levels were calculated using the 2^−ΔΔCt method with GAPDH as the internal reference gene.

Intracellular ROS detection

Intracellular reactive oxygen species (ROS) levels were determined using a DCFH-DA fluorescent probe (Beyotime, China) according to the manufacturer's

instructions. RAW264.7 macrophages were simultaneously treated with lipopolysaccharide (LPS, 1 μg/mL) and different formulations for 24 h. After treatment, the cells were incubated with DCFH-DA in the dark, washed with PBS, and immediately observed under a fluorescence microscope. Intracellular ROS levels were further quantified by flow cytometry.

Mitochondrial membrane potential assay

The mitochondrial membrane potential was evaluated using a JC-1 mitochondrial membrane potential assay kit (Beyotime, China) according to the manufacturer's instructions. RAW264.7 macrophages were simultaneously treated with LPS (1 μg/mL) and different formulations for 24 h. Following treatment, the cells were stained with JC-1 working solution, washed with JC-1 staining buffer, and immediately imaged using a fluorescence microscope. The mitochondrial membrane potential was assessed by calculating the fluorescence intensity ratio of JC-1 aggregates (red fluorescence) to JC-1 monomers (green fluorescence).

Animal experiments and DSS-induced colitis model

All in vivo protocols were strictly executed in compliance with the ethical guidelines and received formal approval from the Medical and Animal Ethics Committee of Northwestern Polytechnical University (Approval Protocol No. 202501087). Male C57BL/6 mice (6–8 weeks old) were housed under specific pathogen-free (SPF) conditions with free access to food and water.

Acute colitis was induced by providing 2.5% (w/v) dextran sulfate sodium (DSS) in the drinking water for 7 consecutive days. Mice were randomly divided into six groups: Control, DSS, DSS + Inulin, DSS + MVs, DSS + MPN@MV, and DSS + Inu@MPN@MV,n = 5 mice per group. Mice in the Control group received normal drinking water and oral gavage of 0.9% NaCl, whereas all DSS-treated groups received 2.5% DSS solution as drinking water. Oral gavage was performed on days 1, 3, 5, and 7 with a total administration volume of 200 μL per mouse. MVs and MPN@MV were administered at an MV dose of 8 mg/kg. Inulin hydrogel was administered at 8 mL/kg, while the Inu@MPN@MV group received Inu@MPN@MV hydrogel at 8 mL/kg containing an equivalent MV dose of 8 mg/kg.

Body weight, stool consistency, and fecal bleeding were recorded daily to calculate the disease activity index (DAI). Mice were sacrificed on day 9, and the colon and major organs were collected for subsequent analyses.

Fluorescence imaging *in vivo*

Dir-labeled MV was orally administered to control and Dss-induced colitis mice. Fluorescence was monitored using an IVIS Spectrum system. At 24 h post-administration, colon was excised for ex vivo imaging.

Histology assay

Colon tissues were harvested immediately after sacrifice, fixed in 4% paraformaldehyde for 48 h, dehydrated through a graded ethanol series, cleared with

xylene, embedded in paraffin, and sectioned into 5 μm slices. Hematoxylin and eosin (H&E) staining was performed to evaluate histopathological changes, while Alcian blue-periodic acid-Schiff (AB-PAS) staining was used to assess goblet cell distribution and mucus secretion. Histological images were acquired using a light microscope. Histological injury was scored according to epithelial damage, crypt loss, inflammatory infiltration, and lesion extent, as described in the scoring criteria provided in the Supporting Information. DAI scoring and histological injury scoring were performed by investigators blinded to the treatment groups.

Biochemical assay

Colon tissues were homogenized in ice-cold lysis buffer and centrifuged to obtain the supernatant. The levels of adenosine triphosphate (ATP), malondialdehyde (MDA), myeloperoxidase (MPO), glutathione (GSH), catalase (CAT), and superoxide dismutase (SOD) were determined using commercial assay kits (Beyotime, China) according to the manufacturer's instructions.

Quantitative Real-Time PCR assay of colon tissue

Total RNA was extracted from colon tissues using a commercial RNA extraction kit according to the manufacturer's instructions. Complementary DNA (cDNA) was synthesized by reverse transcription, and quantitative real-time PCR (qRT-PCR) was performed using a SYBR Green Master Mix. Relative gene expression levels were calculated using the 2^−ΔΔCt method with GAPDH as the internal reference gene.

Gut microbiota assay

Fresh fecal samples were collected aseptically and immediately stored at −80 °C until analysis. Microbial genomic DNA was extracted using a commercial DNA extraction kit according to the manufacturer's instructions. The V3–V4 hypervariable regions of the bacterial 16S rRNA gene were amplified and subjected to paired-end sequencing on an Illumina platform. Sequencing data were processed using standard bioinformatics pipelines to evaluate α-diversity, β-diversity, microbial community composition, and differential taxonomic abundance. Alpha-diversity indices were compared using Kruskal–Wallis tests followed by Dunn's multiple-comparisons test, and beta-diversity differences were assessed by PERMANOVA. Differentially abundant taxa were identified using rank-based tests with Benjamini–Hochberg false-discovery rate (FDR) correction; taxa with FDR-adjusted $p < 0.05$ were considered significant. All sequencing and bioinformatics analyses were performed by Novogene Co., Ltd. (Beijing, China).

Untargeted metabolomics

Fecal samples were collected, immediately frozen in liquid nitrogen, and stored at −80 °C before analysis. Metabolites were extracted using a methanol-based extraction procedure and analyzed by liquid chromatography–mass spectrometry (LC–MS). Raw data were subjected to peak detection, alignment, normalization,

metabolite annotation, and multivariate statistical analyses. Principal component analysis (PCA) and partial least-squares discriminant analysis (PLS-DA) were used to evaluate group separation. Differential metabolites were defined by variable importance in projection (VIP) > 1 and FDR-adjusted $p < 0.05$ after Benjamini–Hochberg correction. KEGG pathway enrichment was evaluated using FDR-adjusted significance thresholds. Untargeted metabolomic analysis was performed by Novogene Co., Ltd. (Beijing, China).

RNA sequencing and transcriptomic assay

Total RNA was extracted from colon tissues, and RNA integrity was evaluated prior to library construction. Sequencing libraries were prepared according to the manufacturer's protocols and sequenced on a high-throughput Illumina platform. Differentially expressed genes (DEGs) were identified using DESeq2; genes with $|\log2(\text{fold change})| \geq 1$ and adjusted $p < 0.05$ after Benjamini–Hochberg correction were considered differentially expressed. Gene Ontology (GO) and Kyoto Encyclopedia of Genes and Genomes (KEGG) enrichment analyses were performed using adjusted $p < 0.05$ as the significance threshold, and gene set enrichment analysis (GSEA) was interpreted using FDR q values. RNA sequencing and downstream bioinformatic analyses were performed by Shanghai Liebing Biotechnology Co., Ltd. (Shanghai, China).

Biosafety evaluation

For the 30-day repeated oral administration safety study, mice received the corresponding formulations according to the long-term dosing schedule. At the end of the observation period, blood samples were collected for routine hematological analysis and serum biochemical assays of hepatic and renal function. Major organs, including the heart, liver, spleen, lung, and kidney, were collected, fixed in 4% paraformaldehyde, embedded in paraffin, sectioned, and stained with hematoxylin and eosin (H&E). Histopathological changes were examined under a light microscope.

Statistical assay

All quantitative data are presented as the mean ± standard deviation (SD). Statistical analyses were performed using GraphPad Prism 9.0 unless otherwise specified. Comparisons between two groups were conducted using an unpaired two-tailed Student's t-test, while comparisons among multiple groups were performed using one-way analysis of variance (ANOVA) followed by Tukey's multiple-comparisons test. Body weight and DAI, which were measured repeatedly over time, were analyzed using two-way repeated-measures ANOVA with treatment and time as factors followed by Sidak's multiple-comparisons test; when missing values were present, a mixed-effects model was used. Omics datasets were analyzed using the differential-analysis and multiple-testing correction methods described in the microbiome, metabolomics, and transcriptomics methods sections. For non-omics analyses, $p < 0.05$ was considered statistically significant; for omics analyses, FDR-adjusted p values or q values were used as indicated.

Results

Construction and characterization of MPN-coated MVs

To engineer MVs with enhanced antioxidant activity while preserving their intrinsic biological properties, MVs were coated with a caffeic acid-Fe^{3+} metal-phenolic network (MPN). TEM images revealed that native MVs exhibited a typical spherical morphology enclosed by an intact lipid membrane. MPN@MV retained this vesicular structure and displayed a thin surface coating, indicating successful deposition of the MPN layer without compromising membrane integrity (Figure 1A). Nanoflow cytometry confirmed the presence of typical extracellular vesicle (EV) markers, including CD9, CD63, and CD81, on the surface of native MVs [15,36] (Figure 1B,C). These membrane-associated markers remained detectable after MPN assembly (Figure 1D,E), showing that the coating process largely preserved the biological identity of the parental vesicles. Dynamic light scattering (DLS) analysis revealed that the hydrodynamic diameter increased from 183.16 ± 5.42 nm for MV to 209.57 ± 4.82 nm after MPN coating, while a narrow particle size distribution was maintained (Figure 1F,G). The surface zeta potential also shifted toward a more negative value (Figure 1H), consistent with assembly of the phenolic coating.

The chemical composition of MPN@MV was then characterized by X-ray photoelectron spectroscopy (XPS). Survey spectra showed characteristic C 1s, N 1s, O 1s, and Fe 2p signals (Figure 1I). High-resolution spectra identified the expected carbon-, nitrogen-, and oxygen-containing chemical environments (Figure 1J-L).

Distinct Fe $2p_{3/2}$ and Fe $2p_{1/2}$ peaks confirmed iron incorporation through caffeic acid-Fe^{3+} coordination (Figure 1M). Elemental mapping revealed homogeneous C, N, O, and Fe signals across individual nanoparticles (Figure 1N), supporting uniform MPN shell formation rather than nonspecific iron aggregation. UV-visible spectroscopy provided another readout of metal-phenolic coordination. Compared with native MV, MPN@MV exhibited absorption bands at approximately 376 and 586 nm, corresponding to ligand-to-metal charge transfer generated by caffeic acid-Fe^{3+} coordination (Figure 1O). Given that polyphenol-based coordination networks are intrinsically redox active [35,37], the antioxidant capacity of MPN@MV was examined using ABTS and DPPH radical scavenging assays. MPN@MV eliminated both radicals in a concentration-dependent manner (Figure 1P,Q). Accordingly, surface engineering with MPN coating endowed MVs with potent antioxidant activity while preserving their structural and biological characteristics.

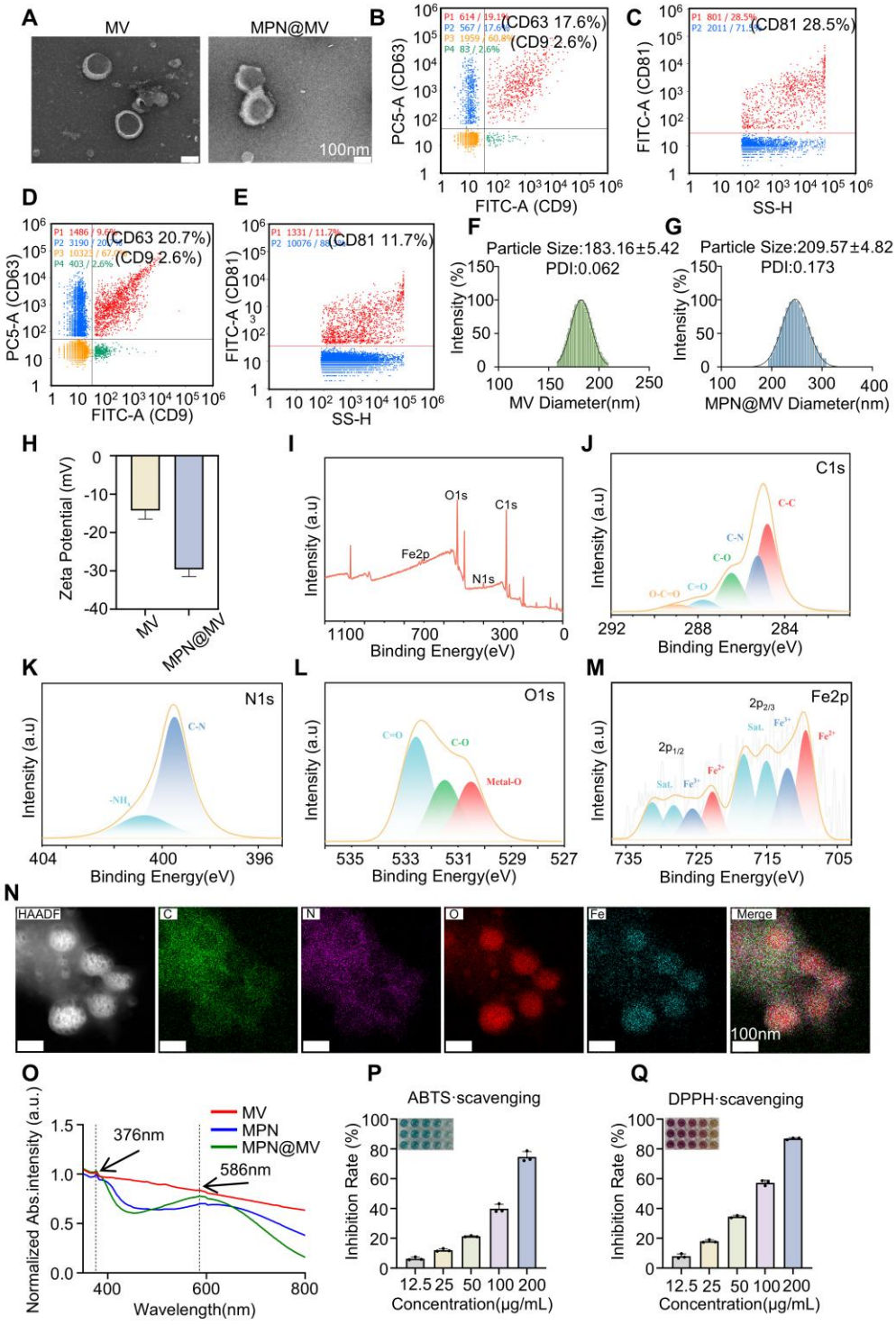


Figure 1. Construction and physicochemical characterization of MPN-coated MVs. (A) TEM images of MV and MPN@MV. (B-E) Nanoflow cytometry analysis of MV and MPN@MV surface markers, including CD9, CD63, and CD81. (F,G)

Hydrodynamic diameter and size distribution of MV and MPN@MV. (H) Zeta potential changes after MPN coating. (I–M) XPS survey and high-resolution spectra. (N) Elemental mapping of MPN@MV. (O) UV-visible absorption spectra showing ligand-to-metal charge transfer bands. (P,Q) ABTS and DPPH radical-scavenging activity of MPN@MV. Data are shown as mean ± SD with n = 3.

MPN@MV modulated macrophage M2 polarization while reducing oxidative injury *in vitro*

Because surface engineering may alter the behavior of MVs [38–40], the cytocompatibility of MPN@MV was first evaluated in RAW264.7 macrophages. CCK-8 assays showed that neither MV nor MPN@MV induced detectable cytotoxicity across the tested concentration range (Figure S1). Live/Dead staining gave the same result, with predominantly viable cells and only minimal dead-cell signals after treatment (Figure S2). Therefore, MPN assembly did not compromise the intrinsic biocompatibility of MVs [13,16,39]. Efficient cellular internalization is required for vesicle-mediated biological activity[13,16]. PKH26-labeled MVs were used to examine macrophage uptake. Confocal microscopy showed comparable intracellular fluorescence in the MV and MPN@MV groups, indicating that MPN coating did not impair the MVs internalization (Figure S3A,B). Notably, LPS stimulation moderately enhanced MVs uptake compared with unstimulated macrophages, consistent with the increased endocytic activity of activated

inflammatory macrophages [5,41]. Therefore, surface engineering preserved the intrinsic cell-interacting properties of MVs.

Given that oxidative stress profoundly influences macrophage polarization and that M2 polarization is directly linked to mucosal repair and immune restoration [41,42], we subsequently evaluated the capacity of MPN@MV to promote M2 macrophage polarization, rather than examining other immune cell subsets. Immunofluorescence staining showed that LPS stimulation strongly increased the expression of the M1 marker CD86 while suppressing the expression of the M2 marker CD206 (Figure 2A-D). However, single MV treatment did not effectively reverse this inflammatory polarization pattern, likely due to LPS-induced accumulation of intracellular ROS that impaired the MV activity. In contrast, MPN@MV produced a stronger reduction in CD86 expression and a more pronounced increase in CD206, pointing to a more effective shift toward an anti-inflammatory macrophage phenotype. Additionally, RT-qPCR analysis supported above-mentioned results. Compared with the MV treatment, MPN@MV markedly downregulated the pro-inflammatory cytokines TNF-α, IL-1β, and IL-6, while increasing the anti-inflammatory cytokine IL-10 in LPS-stimulated macrophages (Figure 2E-H). In addition, the M2-associated marker Arg-1 was also elevated after MPN@MV treatment (Figure S4), further suggesting macrophage repolarization toward a reparative phenotype.

Because excessive ROS is closely coupled with macrophage activation and contributes to persistent inflammatory injury in IBD [41,43,44], we subsequently evaluated whether MPN@MV could alleviate the intracellular oxidative stress. Flow cytometry showed that LPS stimulation sharply increased ROS production, whereas MV treatment only partially reduced ROS accumulation (Figure 2I,J). However, MPN@MV achieved stronger ROS elimination than native MV, attributed to the antioxidant activity introduced by the metal-phenolic coating.

To test whether ROS clearance translated into broader recovery of cellular redox homeostasis, oxidative stress-related biochemical indicators were further quantified. LPS stimulation reduced the intracellular GSH and ATP levels, CAT and SOD activities, while increasing the MDA level and MPO activity (Figure 2K-P), reflecting impaired antioxidant defense, lipid peroxidation, and inflammatory oxidative injury [41,44]. MPN@MV treatment recovered antioxidant capacity, as shown by increased GSH, CAT, ATP, and SOD together with reduced MDA and MPO accumulation. In addition, DCFH-DA fluorescence imaging produced the same trend, with much weaker intracellular ROS signals in the MPN@MV group than in the LPS and MV group (Figure 2Q and Figure S5). JC-1 staining further showed that LPS-induced mitochondrial depolarization was only partially alleviated by native MV, whereas MPN@MV largely preserved mitochondrial membrane potential (Figure S6 A,B). These results demonstrated that the immunomodulatory effect of redox-buffered MVs on macrophages is associated with the restoration of intracellular redox balance and mitochondrial homeostasis mediated by MPN coating.

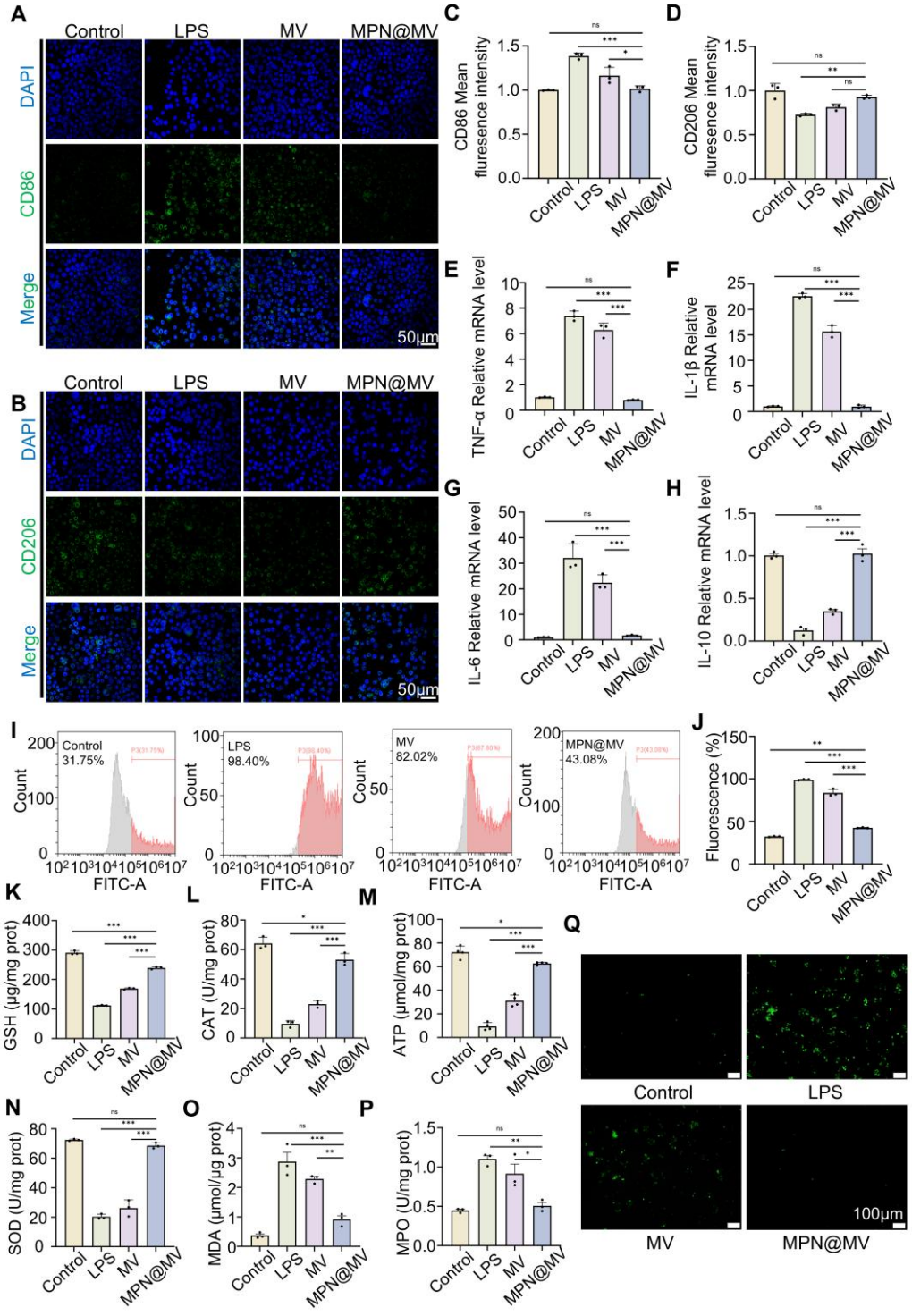


Figure 2. MPN@MV attenuates LPS-induced macrophage activation and oxidative stress in vitro. RAW264.7 macrophages were stimulated with LPS and treated with MV or MPN@MV (MV and MPN@MV: 50 μg/mL). (A–D) Immunofluorescence

staining and quantification of CD86 and CD206. (E–H) qRT-PCR analysis of TNF-α, IL-1β, IL-6 and IL-10. (I,J) Flow-cytometric detection and quantification of intracellular ROS. (K–P) Intracellular oxidative stress and antioxidant indicators, including GSH, CAT, ATP, SOD, MDA and MPO. (Q) Representative DCFH-DA fluorescence images of intracellular ROS. Data are shown as mean ± SD with n = 3.

Inulin hydrogel protected MPN@MV during gastrointestinal transit and enhanced intestinal retention after oral administration

To overcome gastrointestinal degradation and improve the oral delivery efficiency of MPN@MV, an inulin hydrogel was employed as a multifunctional delivery matrix. Scanning electron microscopy revealed a highly interconnected porous architecture that was well preserved after MPN@MV encapsulation (Figure S7). Likewise, the macroscopic appearance of the gel remained unchanged before and after loading (Figure S8), indicating that incorporation of MPN@MV did not interfere with hydrogel formation. The resulting formulation could be smoothly extruded through the gavage needle without visible structural disruption (Figure S9), supporting its practical compatibility with oral gavage. Throughout the tested frequency range, the storage modulus (G′) remained higher than the loss modulus (G″), indicating an elastic-dominant gel network (Figure 3A). During repeated high- and low-strain cycles, both moduli underwent reversible decreases and recovery,

suggesting that the hydrogel possessed recoverable viscoelastic behavior after deformation (Figure 3B).

The pH-dependent degradation behavior of the inulin hydrogel was subsequently evaluated. Because orally administered formulations generally leave the stomach within the first several hours [21,22], particular attention was paid to hydrogel degradation during the initial 6 h. Within this period, the hydrogel exhibited substantially greater mass loss at pH 8.0 than at pH 1.5, whereas a larger proportion of the hydrogel remained intact under the strongly acidic condition during the initial 6 h (Figure 3C). These results indicate that the hydrogel can maintain greater structural integrity during the gastric residence stage while undergoing more rapid degradation under alkaline conditions, thereby favoring subsequent release of the encapsulated MPN@MV after gastrointestinal transit. Consistent with the pH-responsive degradation profile, MPN@MV was progressively released from the hydrogel at pH 8.0. The cumulative release increased rapidly during the early stage and subsequently entered a slower release phase, reaching approximately 85% at 12 h and approaching 90% by the end of the observation period (Figure 3D). This release behavior suggests that alkaline conditions facilitate hydrogel disassembly and the gradual liberation of the encapsulated vesicles. The ability of the hydrogel to protect MPN@MV against gastric damage was further examined after exposure to simulated gastric fluid (SGF). Free MPN@MV exposed directly to SGF showed pronounced structural disruption and irregular particulate morphology. In contrast, particles recovered from SGF-treated Inu@MPN@MV retained a more intact and well-defined vesicle-like

structure (Figure 3E). DLS analysis further showed that the released particles had a hydrodynamic diameter of 213.12 ± 2.69 nm (Figure 3F), which was comparable to that of MPN@MV before hydrogel encapsulation (Figure 1G). Together, these results demonstrate that, although the hydrogel subsequently degrades and releases its cargo under alkaline conditions, it provides effective structural protection for MPN@MV during exposure to the acidic gastric environment.

In addition to providing antioxidant protection, the catechol-rich MPN coating was expected to facilitate inflammation-associated accumulation of MPN@MV through multivalent interactions with the damaged, protein- and mucus-rich mucosal surface of colonic lesions [28,35]. The gastrointestinal retention of orally administered formulations was subsequently evaluated by longitudinal fluorescence imaging at 4, 8, 12, and 24 h after gavage. The analysis included healthy mice receiving Inu@MPN@MV, DSS-treated mice receiving free MVs, and DSS-treated mice receiving Inu@MPN@MV (Figure 3G). Fluorescence signals gradually decreased over time in all three groups, consistent with the progressive gastrointestinal transit and clearance of the administered formulations. In DSS-treated mice receiving free MVs, the fluorescence signal declined more rapidly and only weak residual fluorescence remained at 24 h. By contrast, Inu@MPN@MV produced more persistent signals, which remained readily detectable at both 12 and 24 h. Moreover, the stronger retention observed in DSS-treated mice may be associated with the damaged and protein- or mucus-rich mucosal surface of the inflamed intestine, which could provide additional interaction sites for the phenolic coating

[28,35]. Quantification of the longitudinal imaging results confirmed that the DSS + Inu@MPN@MV group maintained the highest fluorescence intensity throughout the observation period, whereas the DSS + MV group showed the most rapid signal loss (Figure 3I). To further determine the gastrointestinal distribution at the terminal time point, mice were sacrificed at 24 h after administration, and the gastrointestinal tracts were collected for *ex vivo* imaging (Figure 3H). The DSS + Inu@MPN@MV group exhibited the strongest residual fluorescence signal, which was significantly higher than that observed in the DSS + MV group (Figure 3J). Moreover, DSS-treated mice receiving Inu@MPN@MV showed stronger intestinal fluorescence than healthy mice receiving the same formulation, suggesting preferential retention of the hydrogel formulation within the inflamed gastrointestinal tract. *Ex vivo* imaging of the major organs, including the heart, liver, spleen, lung, and kidney, showed no detectable fluorescence signal at 24 h after administration (Figure S10). This distribution pattern suggests that the fluorescently labeled formulation was predominantly retained within the gastrointestinal tract, with no appreciable accumulation in the examined major organs within the detection limit of the imaging system.

Collectively, the inulin hydrogel maintained greater structural integrity during the early acidic exposure stage, promoted MPN@MV release under alkaline conditions, protected the vesicles against SGF-induced structural damage, and prolonged their gastrointestinal retention after oral administration. The absence of detectable fluorescence in the major organs further indicated that the formulation

remained predominantly confined to the gastrointestinal tract during the observation period.

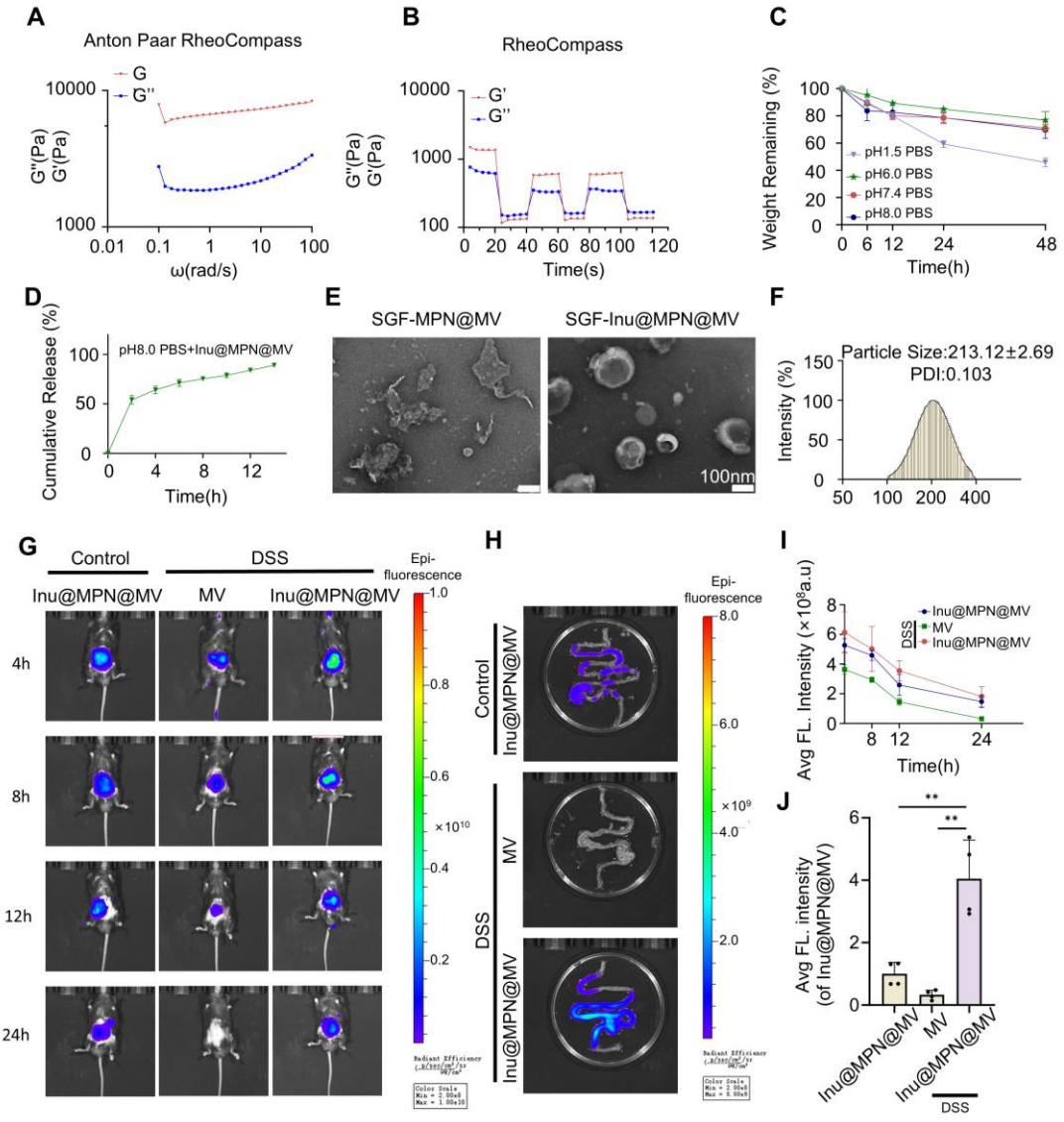


Figure 3. Inulin hydrogel protects MPN@MV and enhances gastrointestinal retention. (A) Frequency-sweep rheological analysis of the inulin hydrogel. (B) Alternating strain test showing self-recovery of the inulin hydrogel network. (C) pH-dependent degradation of Inu@MPN@MV hydrogel under simulated gastrointestinal conditions. (D) Sustained release of MPN@MV under simulated colonic conditions. (E,F) TEM

and DLS characterization of vesicles released after simulated gastric-fluid exposure, supporting preservation of vesicle-like morphology and size distribution after SGF exposure. (G–J) In vivo and ex vivo fluorescence imaging showing enhanced gastrointestinal distribution and prolonged colonic retention after oral administration of Inu@MPN@MV compared with free MPN@MV (n = 4).

Oral Inu@MPN@MV alleviated DSS-induced colitis and restored intestinal barrier structure

Having established that the inulin hydrogel protects MPN@MV during gastrointestinal transit and enhances colonic delivery, we next evaluated therapeutic efficacy in a dextran sulfate sodium (DSS)-induced acute colitis model (Figure 4A). DSS-treated mice developed progressive weight loss accompanied by severe clinical symptoms. DSS exposure induced progressive body-weight loss, increased DAI scores, and pronounced colon shortening, reflecting the development of acute colitis (Figure 4B–D). Oral administration of free MVs only partially alleviated these clinical manifestations, consistent with the limited stability and intestinal retention of unprotected MVs after oral delivery [21–23]. MPN@MV produced a greater improvement than free MVs, suggesting that the MPN coating partially preserved MV function and contributed additional protection against the inflammatory and oxidative colonic environment [9,25,35]. Inulin alone also attenuated body-weight loss and reduced DAI scores, indicating that the hydrogel was not merely an inert carrier but

contributed to intestinal protection. Among the treatment groups, Inu@MPN@MV showed the most consistent improvement in body-weight maintenance and DAI progression (Figure 4B,C). Colon length measurements further showed that Inu@MPN@MV significantly alleviated DSS-induced colon shortening compared with the untreated DSS and MV groups. (Figure 4D,G) Among all treatment groups, Inu@MPN@MV produced the greatest improvement in these macroscopic disease indicators, indicating that the delivery framework enhanced the therapeutic performance of orally administered MVs. Histological examination further corroborated the therapeutic benefits of Inu@MPN@MV. H&E staining revealed severe epithelial disruption, crypt destruction, inflammatory cell infiltration, and extensive mucosal damage in DSS-treated mice (Figure 4E). These pathological alterations were substantially alleviated following Inu@MPN@MV treatment, with preservation of epithelial architecture and restoration of crypt structure. In addition, AB-PAS staining further demonstrated that DSS-induced depletion of mucus-producing goblet cells was effectively reversed, indicating recovery of the intestinal mucus barrier (Figure 4F). Histopathological scoring revealed significantly higher colonic damage in the DSS group compared to controls. Following therapeutic intervention, all treatment groups exhibited reduced histologic scores, with the Inu@MPN@MV group showing the most pronounced attenuation, underscoring its superior efficacy over MV, MPN@MV and Inulin alone (Figure 4H). Masson's trichrome staining further showed that DSS exposure disrupted the normal distribution and organization of colonic collagen fibers, consistent with damage to the

mucosal and submucosal extracellular matrix. Inu@MPN@MV treatment restored a more continuous and regularly organized collagen architecture resembling that of healthy colon tissue (Figure S11), suggesting preservation of extracellular-matrix integrity during mucosal repair.

Because epithelial barrier disruption is a central feature of DSS-induced colitis [1,3,45,46], the distribution of the tight-junction proteins occludin and ZO-1 was subsequently examined. In healthy colonic tissue, both proteins showed relatively strong and continuous staining along the epithelial layer. DSS exposure markedly reduced their fluorescence intensity and disrupted their continuous epithelial distribution (Figure 4I). Free MVs produced only limited recovery, whereas MPN@MV and Inulin partially restored the expression and organization of both tight-junction proteins. The stronger recovery observed after MPN@MV than after free MV treatment may reflect the additional antioxidant and lesion-retention properties introduced by the MPN coating, while the effect of Inulin is consistent with its independent contribution to mucosal protection [29–31]. Inu@MPN@MV produced the most pronounced recovery, restoring a more continuous epithelial distribution of both occludin and ZO-1. Quantitative analysis showed that the positive areas of occludin and ZO-1 were significantly greater in the Inu@MPN@MV group than in the DSS, MV, MPN@MV, and Inulin groups, while no significant difference remained relative to the Control group (Figure 4J,K). These findings indicate that the complete formulation more effectively preserved tight-junction-associated structures

than its individual components.

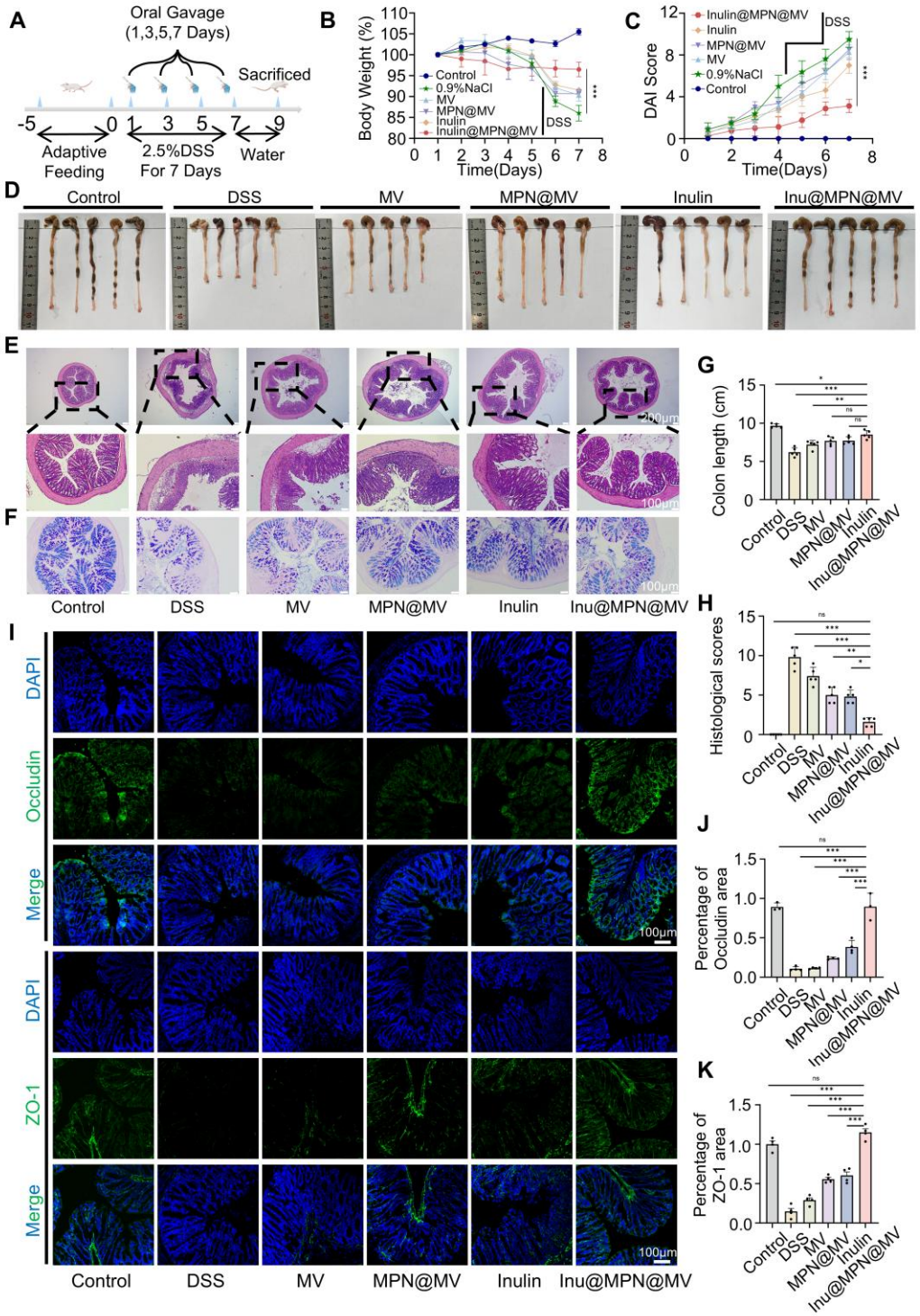


Figure 4. Oral Inu@MPN@MV alleviates DSS-induced colitis and restores epithelial barrier structure. (A) Experimental timeline for DSS-induced acute colitis and oral

treatment. (B,C) Body-weight change and disease activity index. (D) Digital photos of the colons of each group of mice on day 9. (E,F) Representative H&E and AB-PAS staining of colon tissues showing epithelial injury, crypt damage and mucus barrier recovery. (G,H) Quantification of colon length and histological injury scores. (I–K) Immunofluorescence staining and quantification of ZO-1 and occludin. Data are shown as mean ± SD with n = 5.

Inu@MPN@MV reduced inflammatory macrophage activation and oxidative damage in colon tissue

To clarify the *in vivo* mechanisms underlying therapeutic efficacy, macrophage polarization was first examined in inflamed colon tissue. Macrophages are central regulators of intestinal inflammation, facilitating the coordination of immune responses and tissue repair [5]. Immunofluorescence staining of colonic tissues showed that DSS exposure markedly increased the proportion of CD86-positive cells among F4/80-positive macrophages while reducing CD206-positive macrophages, indicating a shift toward a predominantly pro-inflammatory macrophage state (Figure 5A–C). Free MV administration produced only a limited reduction in CD86 and a modest increase in CD206, which may reflect the insufficient protection and retention of orally delivered MVs [21–23]. MPN@MV more clearly reduced the CD86-positive macrophage population and increased CD206 expression, supporting the contribution of the MPN coating to maintaining a more permissive local environment for

MV-mediated immunoregulation [9,25,35]. Inulin alone also moderately altered macrophage-associated staining, although its effect was less pronounced than that of MPN@MV. Inu@MPN@MV produced the greatest increase in CD206-positive macrophages, with the CD206-positive proportion significantly exceeding those of all other groups, including the healthy Control group (Figure 5B). This result therefore reflects a treatment-associated reparative macrophage response rather than simple normalization to the healthy baseline. In contrast, the CD86-positive proportion in the Inu@MPN@MV group was restored to a level comparable to that of the Control group (Figure 5C). The phenotypic transition of macrophages was corroborated by q-PCR analysis of inflammatory mediators. DSS treatment elevated the pro-inflammatory cytokines TNF-α, IL-1β, and IL-6 while suppressing the anti-inflammatory cytokine IL-10 (Figure 5D-G). Inu@MPN@MV downregulated all three pro-inflammatory cytokines and recovered IL-10 expression to levels approaching those of healthy controls. Expression of the M2-associated marker Arg-1 was also increased after Inu@MPN@MV treatment (Figure S12), further suggesting polarization toward a reparative macrophage phenotype.

Since oxidative stress is another major pathological driver of intestinal inflammation [41,44], we next examined local redox homeostasis. DSS administration caused a pronounced reduction in the endogenous antioxidant indicators SOD and GSH, accompanied by elevated MDA and MPO levels (Figure 5H-K). This pattern reflects severe oxidative injury, lipid peroxidation, and impaired antioxidant defense [41,44]. Inu@MPN@MV restored antioxidant capacity by increasing SOD and GSH

while reducing MDA and MPO accumulation. CAT activity, which was markedly impaired after DSS administration, also recovered after Inu@MPN@MV treatment (Figure S13). These biochemical changes are consistent with partial recovery of endogenous antioxidant defenses within inflamed colonic tissues.

The regulation of macrophage polarization and oxidative stress observed *in vivo* closely mirrored the cellular responses identified in RAW264.7 macrophages. This agreement supports that the antioxidant contribution of the MPN shell and the immunomodulatory activity of MVs were at least partly preserved after oral delivery. Inu@MPN@MV partially normalized the inflamed colonic immune microenvironment and redox status, providing a plausible mechanistic basis for the improved epithelial barrier integrity and disease indices observed in DSS-induced colitis. These local effects also raised an important question: whether treatment was accompanied by broader remodeling of the gut microbial ecosystem.

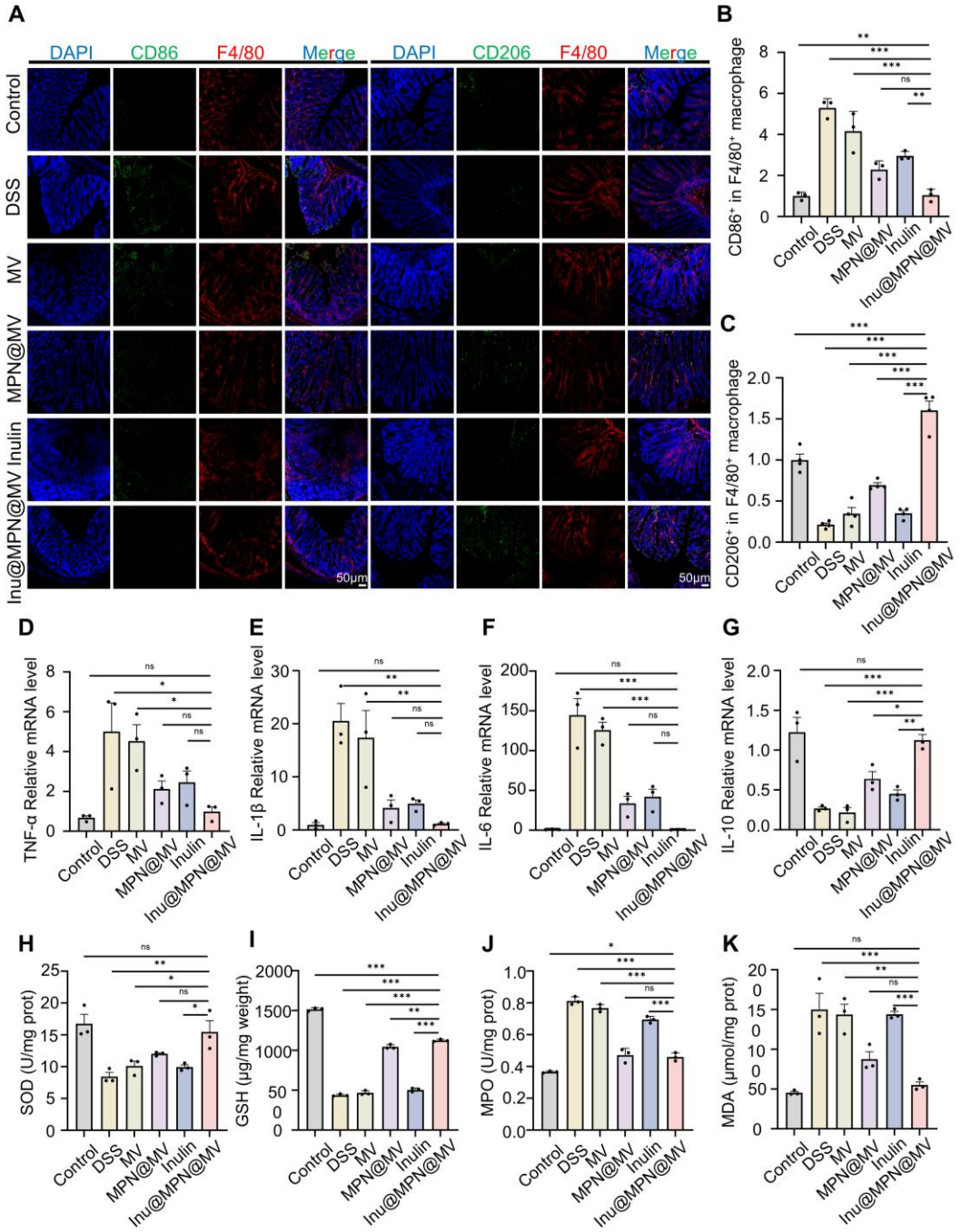


Figure 5. Inu@MPN@MV reduces inflammatory macrophage activation and oxidative injury in colon tissue. (A–C) Immunofluorescence staining and quantification of CD86 and CD206 in colonic sections from Control, DSS and treatment groups. (D–G) qRT-PCR analysis of TNF-α, IL-1β, IL-6 and IL-10 in colon

tissues. (H–K) Biochemical analysis of SOD, GSH, MDA and MPO levels in colonic tissue homogenates. Data are shown as mean ± SD with n = 3.

Inu@MPN@MV is associated with partial restoration of gut microbial composition in DSS-induced colitis.

Because regulation of the intestinal microbial ecosystem is important for intestinal homeostasis and recovery in experimental colitis [45,46], 16S rRNA sequencing was performed to determine whether the local immunomodulatory and antioxidant effects of Inu@MPN@MV were accompanied by broader microbiota remodeling. Venn analysis revealed both shared and group-specific OTUs among the Control, DSS, and Inu@MPN@MV groups (Figure 6A), indicating treatment-associated restructuring of the microbial community. Beta-diversity analyses captured the global impact of different treatments on microbial community structure. Principal coordinate analysis (PCoA), principal component analysis (PCA), and non-metric multidimensional scaling (NMDS) all showed clear separation between the Control and DSS groups, reflecting profound DSS-induced dysbiosis (Figure 6B). Samples from the Inu@MPN@MV group clustered closer to healthy controls than to untreated DSS mice, indicating that oral treatment redirected the intestinal microbiota toward a more normal ecological state.

Changes in microbial diversity were evaluated using α-diversity analyses. DSS administration reduced microbial richness and diversity, as reflected by lower Chao1, Shannon, Simpson, and Pielou's evenness indices (Figure 6C-F). Inu@MPN@MV restored all four diversity indices, indicating recovery of both bacterial richness and community evenness. The phylum-level phylogenetic tree further illustrated broad taxonomic diversity after treatment (Figure S14). Hierarchical clustering heatmaps at the phylum and family levels showed that the microbial composition of Inu@MPN@MV-treated mice more closely resembled healthy controls than untreated DSS mice (Figure S15). Thus, Inu@MPN@MV broadly regulated microbial diversity rather than enriching only a few bacterial taxa.

Taxonomic analysis revealed characteristic shifts in microbial composition. At the phylum level, DSS disrupted the relative abundance of the dominant bacterial phyla, whereas Inu@MPN@MV largely recovered their distribution toward that observed in healthy mice (Figure 6G). Similar recovery appeared at the family level (Figure 6H), indicating remodeling of the intestinal microbial community across multiple taxonomic levels. Differential taxa were then examined at the phylum, family, and genus levels (Figure 6I-N). At the phylum level, DSS increased the relative abundance of Bacteroidota, whereas Inu@MPN@MV reduced it to a level comparable to that of healthy controls (Figure 6I), suggesting correction of a DSS-associated compositional imbalance. Conversely, Actinomycetota was depleted after DSS exposure but markedly enriched following treatment (Figure 6J). This increase was accompanied by a pronounced enrichment of Bifidobacterium (Figure

6N), which is consistent with the fermentation of the inulin matrix and the establishment of a carbohydrate-fermenting microbial environment [29,30,47]. At the family level, Erysipelotrichaceae decreased after DSS exposure and showed recovery following treatment (Figure 6K). Lachnospiraceae exhibited a DSS-associated increase that was reversed by Inu@MPN@MV (Figure 6L). Given the functional heterogeneity of this family [6,7,46], this change is more appropriately interpreted as correction of the DSS-disrupted community structure rather than depletion of beneficial bacteria. Lactobacillaceae, which was markedly reduced by DSS, recovered to a level comparable to that of the Control group after treatment (Figure 6M). The recovery of Lactobacillaceae, together with the enrichment of Bifidobacterium, suggests enhanced fermentative and barrier-supporting potential within the intestinal microbial community [47–50]. Meanwhile, the Verrucomicrobiota also showed a downward trend (Figure S16), further indicating that the treatment with Inu@MPN@MV restored the intestinal homeostasis and was close to that of healthy mice.

Collectively, Inu@MPN@MV corrected several DSS-associated taxonomic alterations while selectively enriching inulin-responsive bacterial populations, supporting a prebiotic-driven remodeling of the intestinal microbiota [29,30,47] rather than uniform restoration of all taxa.

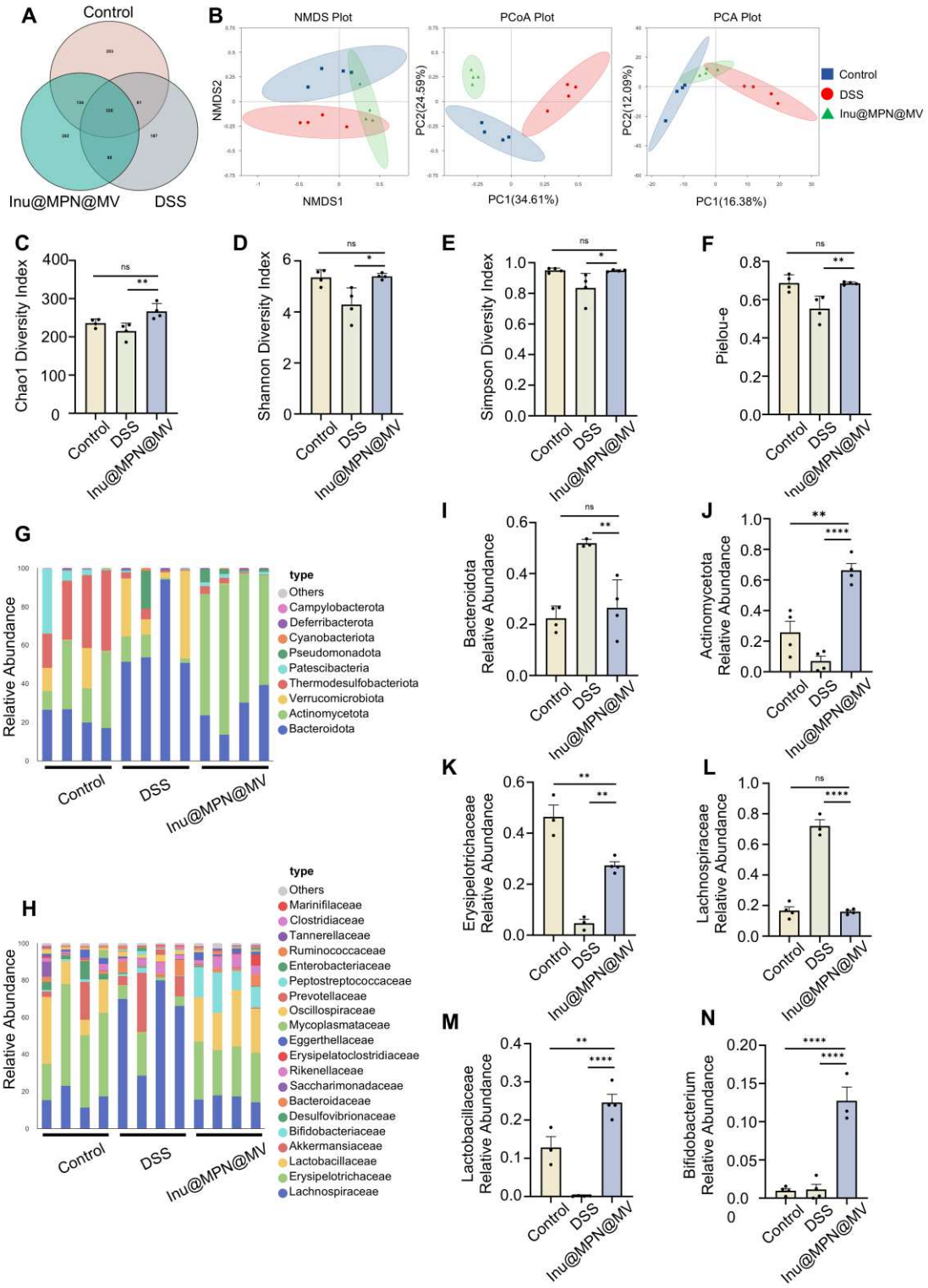


Figure 6. Inu@MPN@MV is associated with partial restoration of gut microbial composition in DSS-induced colitis. (A) Venn analysis of shared and unique OTUs among Control, DSS and Inu@MPN@MV groups. (B) Beta-diversity analysis by

PCoA, PCA and NMDS. (C–F) Alpha-diversity indices, including Chao1, Shannon, Simpson and Pielou's evenness. (G,H) Relative bacterial composition at phylum and family levels. (I–N) Differential taxa and representative genera/families associated with treatment response, including enrichment of beneficial bacteria and reduction of inflammation-associated taxa. Data indicate treatment-associated partial restoration of microbial diversity and community composition after Inu@MPN@MV treatment.Data are shown as mean ± SD with n = 4.

Metabolomics reveals treatment-associated changes in lipid, tryptophan, bile-acid, and redox-related metabolism.

Because gut microbial changes often act through metabolic remodeling [10,46,51,52], untargeted metabolomics was performed to determine whether Inu@MPN@MV altered the fecal metabolic profile of DSS-induced colitis mice. The Venn diagram showed the shared and comparison-specific differential metabolites identified in the Control versus DSS, DSS versus Inu@MPN@MV, and Control versus Inu@MPN@MV comparisons (Figure 7A). DSS challenge markedly disturbed intestinal metabolism, whereas Inu@MPN@MV generated a metabolic profile that partially overlapped with healthy controls while retaining treatment-specific metabolites. These findings indicate that the treatment produced a metabolic profile distinct from DSS and partially closer to the Control group. Multivariate analysis suggested the presence of metabolic remodeling. PCA showed clear separation

between the Control and DSS groups, reflecting broad metabolic disruption after colitis induction (Figure 7B). The Inu@MPN@MV group shifted away from the DSS cluster and toward the Control group, indicating partial normalization of the fecal metabolome. PLS-DA analysis showed even clearer discrimination among groups, supporting the presence of treatment-responsive metabolic features. These results reveal substantial reprogramming of the metabolic landscape associated with intestinal inflammation.

Differential-metabolite analysis identified 629 increased and 336 decreased metabolites in DSS-treated mice relative to healthy controls. Compared with the DSS group, Inu@MPN@MV treatment increased 229 metabolites and decreased 501 metabolites (Figure 7C), indicating broad metabolic remodeling dominated by treatment-associated decreases. Correlation-network analysis further showed extensive positive and negative associations among differential metabolites from several chemical classes (Figure 7D). The metabolic response to Inu@MPN@MV involved multiple interconnected pathways. KEGG pathway enrichment analysis provided a pathway-level view of these changes (Figure 7E). The enriched pathways were mainly associated with lipid metabolism, ferroptosis, glutathione metabolism, primary bile acid biosynthesis, and bile secretion. These pathways are closely linked to intestinal inflammation, oxidative stress, epithelial barrier function, and host-microbiota communication [9,10,46]. Arachidonic acid metabolism is relevant because it generates prostaglandins and other eicosanoids that regulate inflammatory signaling [53]. Linoleic acid metabolism is connected with lipid peroxidation and

oxidized lipid mediator production under inflammatory conditions [44,53]. Tryptophan metabolism provides a bridge between gut microbiota and mucosal immunity, as microbial tryptophan derivatives can regulate epithelial repair and immune tolerance [51,54,55]. Bile acid metabolism is tightly coupled to microbial composition and intestinal barrier homeostasis [52,56]. These pathway shifts indicate that Inu@MPN@MV was associated with changes in both bacterial composition and downstream metabolic signals related to mucosal inflammation.

Among the differential metabolites, arachidonic acid was increased after DSS treatment and reduced following Inu@MPN@MV administration (Figure 7F). Because arachidonic acid is the precursor for multiple pro-inflammatory eicosanoids [53], its reduction is consistent with suppression of lipid mediator-driven inflammation. Linoleic acid was also dysregulated in DSS-induced colitis and partially normalized after treatment (Figure 7G). Disturbed polyunsaturated fatty acid metabolism can promote lipid oxidation and inflammatory signaling [44,53], Therefore, the recovery of linoleic acid metabolism agrees with the reduced oxidative injury observed in colon tissues. Amino acid-related metabolites also showed treatment-responsive changes. L-Tryptophan was restored by Inu@MPN@MV treatment (Figure 7H), suggesting recovery of microbial-host tryptophan metabolism. This is relevant because tryptophan-derived indole metabolites participate in epithelial barrier maintenance and immune regulation [51,54,55]. Consistently, indole-3-butyric acid, a microbial tryptophan-derived metabolite [55], increased after Inu@MPN@MV administration (Figure 7J), supporting recovery of beneficial microbial metabolic

activity. These changes align with the 16S rRNA sequencing results showing enrichment of beneficial bacteria after treatment. Inflammation-associated lipid mediators were also modulated. PGF2α, a prostaglandin derived from arachidonic acid metabolism [53], was decreased in DSS-treated mice but elevated after Inu@MPN@MV treatment (Figure 7I). This result suggests rebalancing of arachidonic-acid-derived lipid mediators rather than uniform suppression of prostaglandin production. Imidazolepropionic acid displayed a similar pattern: its abundance decreased in the DSS group but increased markedly after Inu@MPN@MV treatment and was not significantly different from the Control level (Figure 7K). Therefore, this change should be interpreted as treatment-associated remodeling of microbial histidine-derived metabolism [57] rather than a reduction in a harmful microbial metabolite. Additional metabolites further supported recovery of intestinal metabolic homeostasis. Allocholic acid, a bile acid-related metabolite, was altered by Inu@MPN@MV treatment (Figure S17), suggesting that the formulation influenced bile acid metabolism, likely through microbiota remodeling. Because bile acids can regulate epithelial barrier function and immune responses through host receptors [52,56], this change agrees with the observed barrier repair and reduced inflammation. L-Phenylalanine was also modulated after treatment (Figure S18), indicating that aromatic amino acid metabolism was affected by DSS injury and partially corrected by Inu@MPN@MV.

The metabolomic results are consistent with a functional metabolic response accompanying the treatment-associated microbial changes. Inu@MPN@MV

regulated inflammatory lipid mediators, microbial tryptophan-derived metabolites, bile acid-related metabolism, and aromatic amino acid metabolism. These changes suggest an association between microbial community shifts, metabolic normalization, and the improved inflammatory and barrier phenotypes observed *in vivo*. Together, these data support a working model in which microbial and metabolic recovery accompanied MV-centered immunoregulation within an MPN-buffered, inulin-supported intestinal environment.

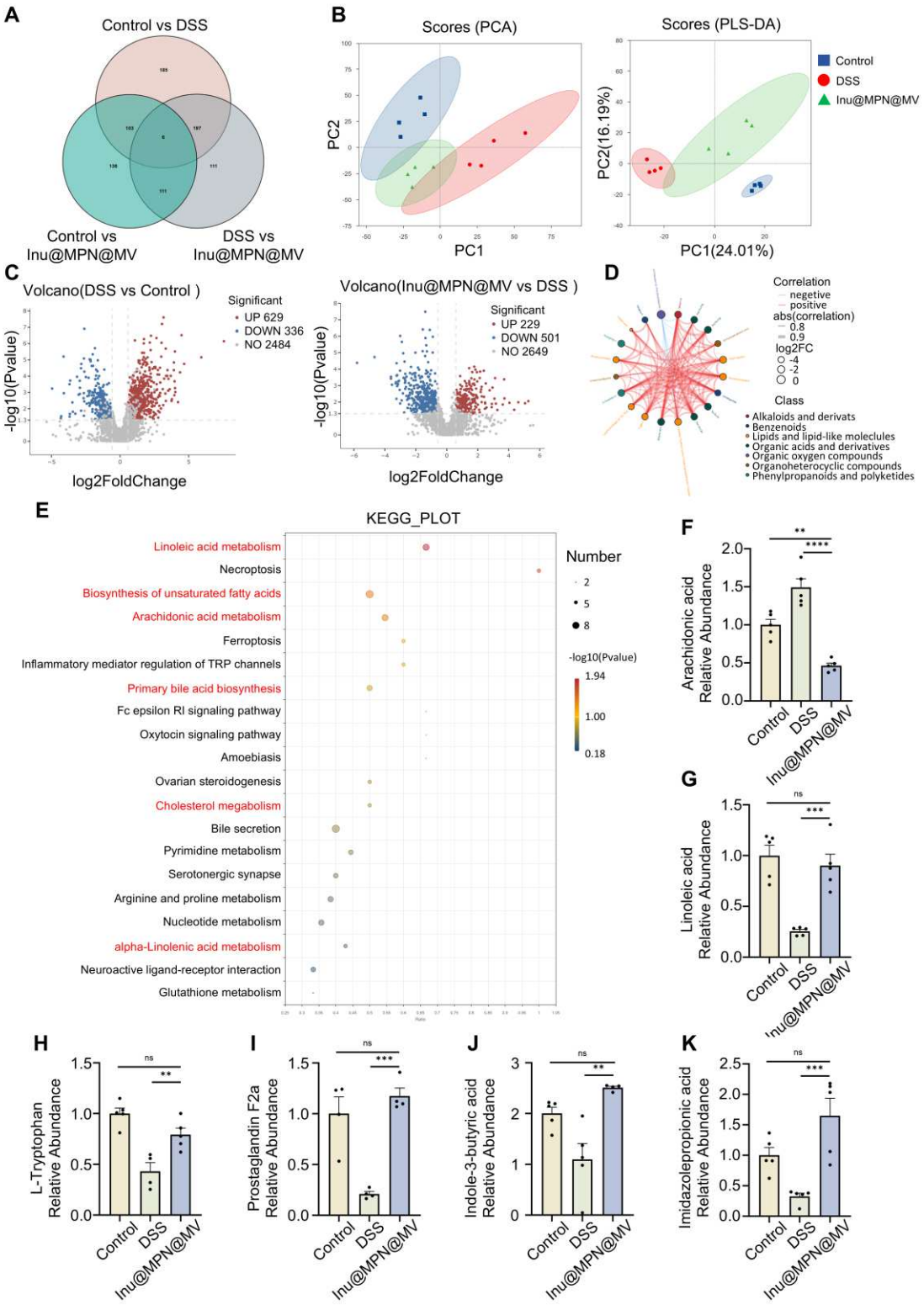


Figure 7. Metabolomics reveals treatment-associated changes in lipid, tryptophan, bile-acid and redox-related metabolism. (A) Venn analysis of fecal metabolites among Control, DSS and Inu@MPN@MV groups. (B) PCA and PLS-DA showing

treatment-associated shifts in the fecal metabolome. (C) Volcano plots of differential metabolites. (D) Metabolite interaction network highlighting hub metabolites involved in inflammatory and microbial metabolic pathways. (E) KEGG enrichment analysis of treatment-responsive metabolic pathways. (F–K) Representative metabolites, including arachidonic acid, linoleic acid, L-tryptophan, PGF2α, indole-3-butyric acid and imidazole propionic acid. Data support treatment-associated metabolic normalization. Data are shown as mean ± SD with n = 5.

Transcriptomics suggested suppression of inflammatory signaling and recovery of metabolic programs

To define the host response underlying Inu@MPN@MV therapy, transcriptomic sequencing was performed using colonic tissues from the Control, DSS, and Inu@MPN@MV groups. Hierarchical clustering analysis showed distinct global transcriptional profiles among the three groups (Figure 8A). Compared with healthy controls, DSS administration induced extensive transcriptional reprogramming. Inu@MPN@MV shifted the overall gene-expression profile toward that of the Control group, indicating broad recovery of host transcriptional homeostasis. Venn analysis illustrated both the overlap and specificity of differentially expressed genes among the experimental groups (Figure 8B). Compared with the Control group, DSS exposure resulted in 1,102 upregulated and 716 downregulated genes (Figure 8C). In contrast, only 133 genes were upregulated and 265 were downregulated in the

Inu@MPN@MV group relative to the Control group (Figure 8D), supporting a reduced overall transcriptional deviation from the healthy state. Compared with DSS-treated mice, Inu@MPN@MV administration upregulated 643 genes and downregulated 1,310 genes (Figure 8E), demonstrating broad treatment-associated transcriptional remodeling with a predominance of downregulated genes.

Gene Ontology (GO) enrichment analysis was performed to characterize the biological functions associated with these transcriptional changes (Figure 8F). The most enriched biological processes included inflammatory response, response to lipopolysaccharide, immune response, innate immune response, neutrophil chemotaxis, and response to bacterium. These signatures are consistent with broad suppression of the excessive immune activation induced by DSS. In parallel, biological processes associated with extracellular matrix organization, cell adhesion, wound healing, collagen fibril organization, and angiogenesis were enriched, in agreement with activation of tissue remodeling and mucosal repair programs [58]. These transcriptional alterations closely match the histological recovery, tight junction restoration, and reduced inflammatory infiltration observed in Figure 4. KEGG pathway analysis revealed regulation of multiple inflammation- and barrier-related signaling pathways (Figure 8G). Among the enriched pathways, cytokine-cytokine receptor interaction, IL-17 signaling [59], complement and coagulation cascades, ECM-receptor interaction, cell adhesion molecules, phagosome, and bile secretion were particularly prominent. Meanwhile, enrichment of ECM-receptor interaction and cell adhesion molecule pathways is consistent with restoration of epithelial barrier

integrity, as shown by histology and tight junction protein expression. Regulation of the bile secretion pathway aligns with the metabolomic recovery of bile acid-related metabolism (Figure 7), highlighting host-microbiota interactions during intestinal repair [46].

Gene Set Enrichment Analysis (GSEA) was used to determine the directionality of pathway regulation (Figure 8H). NF-κB signaling was strongly activated in DSS-treated mice but markedly suppressed after Inu@MPN@MV administration. Because NF-κB is a master regulator of inflammatory gene transcription [60,61], inhibition of this pathway explains the reduced TNF-α, IL-1β, and IL-6 expression observed both *in vitro* and *in vivo*. The TNF signaling pathway, which amplifies inflammatory responses through multiple downstream cascades [4,61,62], showed the same enrichment pattern. JAK-STAT signaling was also inhibited after treatment, further supporting the observed transition of macrophages from a pro-inflammatory to a reparative phenotype [41,62]. GSEA also revealed enrichment of the primary bile acid biosynthesis pathway after Inu@MPN@MV treatment. Bile acids have emerged as important signaling molecules linking gut microbiota to host immunity and epithelial barrier function [52,57]. Recovery of this pathway is consistent with both the 16S rRNA sequencing results demonstrating regulation of the intestinal microbial ecosystem and the metabolomic data indicating normalization of bile acid-related metabolites. These data suggest that inulin-associated microbial changes may be accompanied by partial recovery of microbiota-dependent metabolic communication with the host. Additional GSEA analyses showed regulation of several

metabolism-related pathways (Figure S19). Suppression of the AGE-RAGE signaling pathway is consistent with attenuation of oxidative stress-associated inflammatory injury [41,44], in line with the recovery of redox homeostasis observed in cultured macrophages and inflamed colonic tissues. Enrichment of fatty acid metabolism, the tricarboxylic acid (TCA) cycle, and energy metabolism points to recovery of cellular bioenergetics required for epithelial regeneration, tissue repair, and resolution of inflammation [46,58].

Transcriptomic sequencing further placed the host response within the same treatment-associated framework. Inu@MPN@MV shifted colonic transcriptional profiles, with reduced enrichment of inflammatory signaling pathways and increased representation of repair- and metabolism-related programs. Alongside the microbiome and metabolomic analyses, these data are consistent with a linked microbiota-metabolite-host response in which inulin-associated microbial remodeling is accompanied by metabolic reprogramming and changes in host inflammatory and repair-associated signaling pathways.

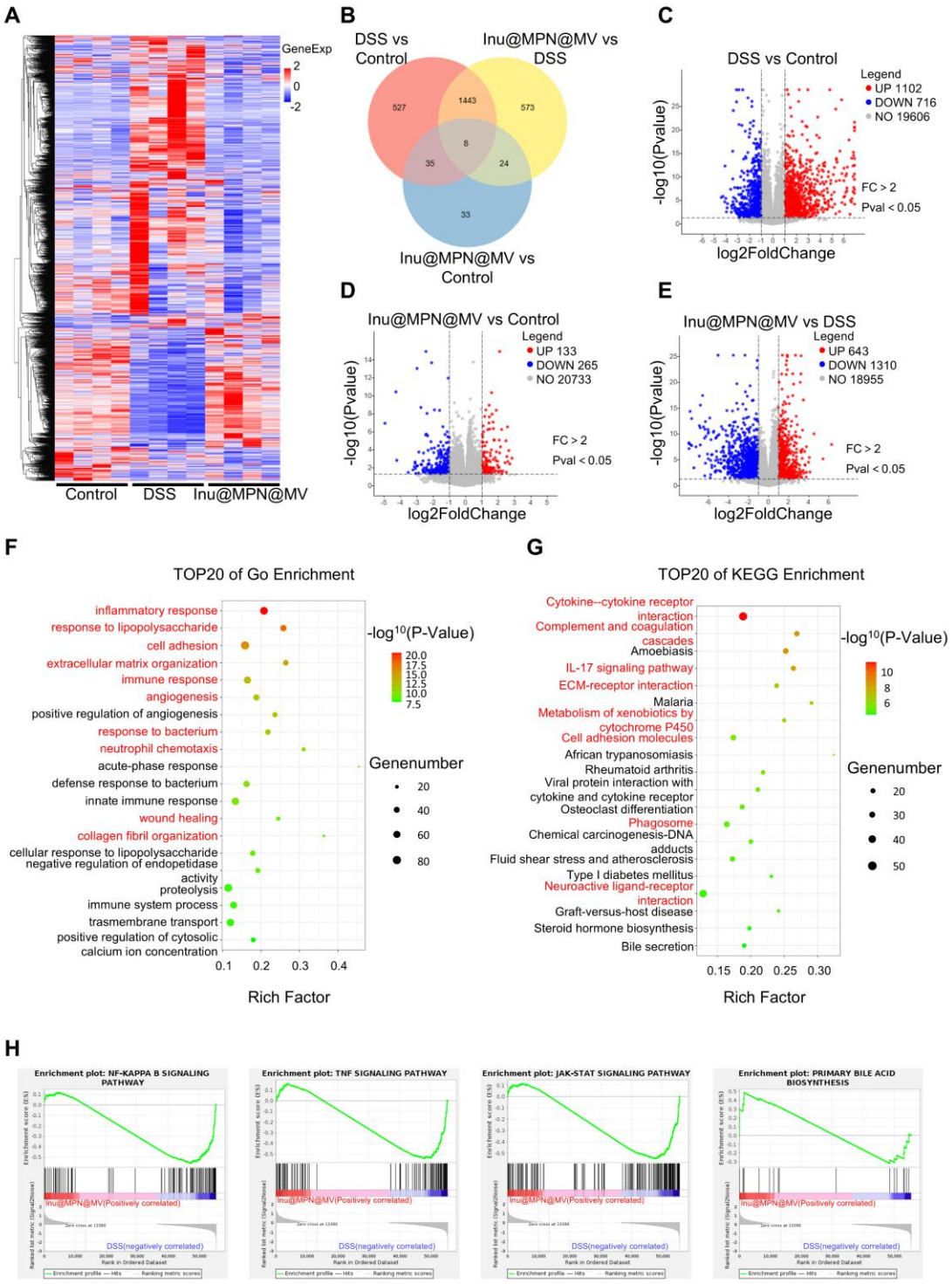


Figure 8. Transcriptomic analysis shows treatment-associated suppression of inflammatory signaling and partial recovery of repair-associated host programs after Inu@MPN@MV treatment. (A) Hierarchical clustering of colon transcriptomic

profiles. (B) Venn analysis of differentially expressed genes. (C–E) Volcano plots and differential gene-expression analyses comparing Control, DSS and Inu@MPN@MV groups. (F) GO enrichment analysis. (G) KEGG enrichment analysis. (H) GSEA showing inhibition of NF-κB, TNF and JAK-STAT signaling and recovery of metabolism-related pathways. Data are shown as mean ± SD with n = 5.

Biosafety after repeated oral administration

Given the intended application of Inu@MPN@MV as an orally administered therapeutic, we further evaluated its preliminary 30-day *in vivo* safety after repeated oral administration. Histological examination of the heart, liver, spleen, lung, and kidney revealed normal tissue architecture without detectable inflammatory infiltration, hemorrhage, necrosis, or other pathological abnormalities in any treatment group (Figure S20), indicating that repeated administration did not induce apparent organ toxicity within the tested observation window. Systemic safety was further assessed by routine hematological and serum biochemical analyses. All hematological parameters remained within the normal physiological range after treatment, with no significant differences compared with healthy controls (Figures S21 and S22). Likewise, serum biochemical markers associated with hepatic and renal function showed no evidence of treatment-related abnormalities. Collectively, these findings indicate that repeated oral administration of Inu@MPN@MV for 30 days was well tolerated *in vivo* and showed no obvious organ toxicity in the tested window,

supporting further evaluation of this platform for chronic oral treatment of inflammatory bowel disease.

Discussion

Oral MV delivery is attractive for IBD because it can deliver therapeutics directly to diseased intestinal tissues while avoiding the burden and systemic exposure associated with repeated injections **[21–23]**. Most reported oral MV systems, however, are designed primarily to improve gastrointestinal stability and delivery efficiency **[21–23]**. They protect MVs during transit, but the delivery materials themselves often contribute little after the MVs reach the colon **[39]**. This limitation significantly compromises the therapeutic efficacy of MV in the treatment of IBD, where intestinal inflammation is sustained not only by immune activation, but also by oxidative stress, epithelial barrier disruption, and gut microbiota dysbiosis **[63]**. Improving delivery alone is unlikely to fully exploit oral MV therapy **[39]**. Therefore, our research demonstrates that Inu@MPN@MV exhibits stronger effects than natural MV on intracellular ROS, mitochondrial membrane potential, macrophage polarization, and inflammatory cytokines, making it suitable for oral delivery of MVs for IBD treatment.

A key feature of this strategy is the integration of multiple therapeutic mechanisms into one oral platform. The inulin hydrogel protects MVs from gastric degradation, enables colon-responsive release, and functions as a prebiotic matrix. Previous studies have shown that inulin promotes beneficial microorganisms,

particularly *Bifidobacterium* and *Lactobacillus*, and thereby improves intestinal barrier function and immune homeostasis [47,48]. Our 16S rRNA sequencing data showed that *Bifidobacterium* was nearly undetectable in both healthy and DSS-treated mice but became readily detectable after Inu@MPN@MV administration. This observation suggests that the hydrogel remained biologically active after oral administration and continued to regulate the microbiota after completing its delivery role. At the same time, the caffeic acid-Fe^{3+} MPN shell not only allowed for the targeting enrichment of MVs to the inflamed lesions, but also endowed MV with antioxidant activity without altering MV morphology, membrane protein expression, or cellular uptake. It effectively mitigated the oxidative damage to MVs caused by the pathological microenvironment. The MPN shell and MV core acted cooperatively to suppress macrophage activation, reduce inflammatory cytokine production, preserve mitochondrial function, and recover intracellular redox homeostasis.

The multi-omics analyses place these material functions into a broader biological context. Gut microbiota sequencing showed that orally-administered Inu@MPN@MV could regulate the microbial diversity and community composition. Metabolomics revealed changes in lipid metabolism, tryptophan metabolism, and bile acid-related pathways, whereas transcriptomics showed reduced enrichment of NF-κB, TNF, and JAK-STAT signaling together with increased representation of repair- and metabolism-related programs. These datasets should not be interpreted as independent proof of a causal microbiota–metabolite–host axis. Rather, they support a coordinated treatment-associated response in which inulin-associated microbial changes,

metabolic normalization, and host inflammatory signaling changes occur in parallel with barrier repair and disease alleviation.

Several limitations should be noted. First, the therapeutic efficacy of Inu@MPN@MV was evaluated mainly in an acute DSS-induced colitis model, which does not fully represent chronic or relapsing IBD. Second, although 16S rRNA sequencing, untargeted metabolomics, and transcriptomics showed coordinated treatment-associated changes, these datasets establish associations rather than direct causality among microbiota remodeling, metabolic normalization, and host inflammatory signaling. Future studies using fecal microbiota transplantation, antibiotic-depletion models, or gnotobiotic animals will be needed to define the causal contribution of gut microbiota. Finally, although the 30-day repeated-dose study showed no obvious systemic toxicity, longer-term safety, immunogenicity, and iron-related metabolic effects of the caffeic acid-Fe^{3+} MPN shell require further evaluation.

This study shows that rational integration of an active prebiotic hydrogel, an antioxidant metal-phenolic coating, and immunoregulatory MVs enables oral MV therapy to move beyond conventional delivery. By allowing the carrier to participate directly in disease modulation and better protect the MV, thereby enabling it to exert its function more effectively, Inu@MPN@MV offers a design principle for next-generation oral MV therapeutics and a promising strategy for treating inflammatory bowel disease.

Conclusion

In summary, we developed Inu@MPN@MV as an MV-centered oral formulation for IBD therapy. MVs served as the principal immunoregulatory effector, while the caffeic acid-Fe^{3+} MPN shell and inulin hydrogel protected MV delivery and reduced environmental constraints on MV activity. The formulation preserved MV identity and uptake, improved gastrointestinal stability and colonic retention, buffered oxidative stress, promoted reparative macrophage polarization, and restored epithelial and mucus barriers in DSS-induced colitis. Integrated microbiome, metabolome, and transcriptome analyses were consistent with a connected microbiota-metabolite-host response involving beneficial and fermentative taxa, normalization of inflammatory lipid, tryptophan, and bile-acid-related metabolism, suppression of major inflammatory pathways, and recovery of barrier-repair and energy-metabolism programs. these findings support material engineering as a means to maintain MV bioavailability and create an intestinal microenvironment favorable for MV-mediated therapy.

ASSOCIATED CONTENT

Ethics approval and consent to participate

All the animal experiments were strictly executed in compliance with the ethical guidelines and received formal approval from the Medical and Animal Ethics Committee of Northwestern Polytechnical University (Approval Protocol No. 202501087).

Notes

The authors declare no competing financial interest.

ACKNOWLEDGMENTS

This work was supported by the Qin Chuangyuan High-Level Innovation and Entrepreneurship Talent Recruitment Program of Shaanxi (QCYRCXM-2023-073) and the Fundamental Research Funds for the Central Universities at Northwestern Polytechnical University (G2022WD01010).

During the preparation of this manuscript, the authors used ChatGPT (OpenAI) to assist with English-language editing, text organization, and improvement of readability. All generated output was critically reviewed and revised by the authors, who take full responsibility for the accuracy and integrity of the final manuscript.

Supporting Information

Additional experimental details; characterization of extracellular vesicles, metal‑phenolic coatings, and inulin hydrogels; cytocompatibility, cellular uptake, macrophage polarization, redox, and mitochondrial assays; gastrointestinal distribution and retention; histological analyses; microbiome, metabolomic, transcriptomic, and repeated-dose safety results; primer sequences; antibody and reagent information; and disease activity and histological scoring criteria (PDF).

AUTHOR INFORMATION

Corresponding Authors

Chenghu Hu — Xi'an Key Laboratory of Stem Cell and Regenerative Medicine, School of Life Science and Technology, Northwestern Polytechnical University, Xi'an, Shaanxi 710072, P. R. China;

Yuan Zhang — Xi'an Key Laboratory of Stem Cell and Regenerative Medicine, School of Life Science and Technology, Northwestern Polytechnical University, Xi'an, Shaanxi 710072, P. R. China;

Chengbiao Hu — Xi'an Key Laboratory of Stem Cell and Regenerative Medicine, School of Life Science and Technology, Northwestern Polytechnical University, Xi'an, Shaanxi 710072, P. R. China;

Author Contributions

Q.P.: [Conceptualization, Methodology, Investigation, Formal Analysis, Data Curation, Visualization, Writing – Original Draft]. P.L.: [Methodology and investigation, and writing review and editing]. Y.G.: [Conceptualization, validation and writing review and editing]. N.Z.: [Visualization and validation]. M.Y.: [Investigation]. Z.W.: [Investigation]. X.F.: [Investigation]. C.H.: [Conceptualization, supervision, writing review and editing and funding acquisition]. Y.Z.: [Conceptualization, supervision, writing review and editing and funding acquisition]. C.H.: [Conceptualization, supervision, writing review and editing and funding acquisition].

All authors reviewed and approved the final version of the manuscript.

ORCID

Chenghu Hu: 0000-0003-2443-6485

References

1. Le Berre C, Honap S, Peyrin-Biroulet L. Ulcerative colitis. The Lancet. 2023;402:571–84. https://doi.org/10.1016/S0140-6736(23)00966-2

2. Roda G, Chien Ng S, Kotze PG, Argollo M, Panaccione R, Spinelli A, et al. Crohn's disease. Nat Rev Dis Primers. Nature Publishing Group; 2020;6:22. https://doi.org/10.1038/s41572-020-0156-2

3. Pathophysiology of Inflammatory Bowel Diseases | NEJM. New England Journal of Medicine [Internet]. [cited 2026 July 9]; https://www.nejm.org/doi/full/10.1056/NEJMra2002697. Accessed 9 July 2026

4. Neurath MF. Strategies for targeting cytokines in inflammatory bowel disease. Nat Rev Immunol. Nature Publishing Group; 2024;24:559–76. https://doi.org/10.1038/s41577-024-01008-6

5. Hegarty LM, Jones G-R, Bain CC. Macrophages in intestinal homeostasis and inflammatory bowel disease. Nat Rev Gastroenterol Hepatol. Nature Publishing Group; 2023;20:538–53. https://doi.org/10.1038/s41575-023-00769-0

6. Shan Y, Lee M, Chang EB. The Gut Microbiome and Inflammatory Bowel Diseases. Annual Review of Medicine. Annual Reviews; 2022;73:455–68. https://doi.org/10.1146/annurev-med-042320-021020

7. de Vos WM, Tilg H, Van Hul M, Cani PD. Gut microbiome and health: mechanistic insights. Gut. 2022;71:1020–32. https://doi.org/10.1136/gutjnl-2021-326789

8. Collins SL, Stine JG, Bisanz JE, Okafor CD, Patterson AD. Bile acids and the gut microbiota: metabolic interactions and impacts on disease. Nat Rev Microbiol. Nature Publishing Group; 2023;21:236–47. https://doi.org/10.1038/s41579-022-00805-x

9. Huang Y, Xu J, Sun G, Cheng X, An Y, Yao X, et al. Enteric-coated cerium dioxide nanoparticles for effective inflammatory bowel disease treatment by regulating the redox balance and gut microbiome. Biomaterials. 2025;314:122822. https://doi.org/10.1016/j.biomaterials.2024.122822

10. Lavelle A, Sokol H. Gut microbiota-derived metabolites as key actors in inflammatory bowel disease. Nat Rev Gastroenterol Hepatol. Nature Publishing Group; 2020;17:223–37. https://doi.org/10.1038/s41575-019-0258-z

11. Tieu A, Lalu MM, Slobodian M, Gnyra C, Fergusson DA, Montroy J, et al. An Analysis of Mesenchymal Stem Cell-Derived Extracellular Vesicles for Preclinical Use. ACS Nano. American Chemical Society; 2020;14:9728–43. https://doi.org/10.1021/acsnano.0c01363

12. Zhang Y, Chen J, Fu H, Kuang S, He F, Zhang M, et al. Exosomes derived from

3D-cultured MSCs improve therapeutic effects in periodontitis and experimental colitis and restore the Th17 cell/Treg balance in inflamed periodontium. Int J Oral Sci. Nature Publishing Group; 2021;13:43. https://doi.org/10.1038/s41368-021-00150-4

13. Kalluri R, LeBleu VS. The biology, function, and biomedical applications of exosomes. Science. American Association for the Advancement of Science; 2020;367:eaau6977. https://doi.org/10.1126/science.aau6977

14. van Niel G, D'Angelo G, Raposo G. Shedding light on the cell biology of extracellular vesicles. Nat Rev Mol Cell Biol. Nature Publishing Group; 2018;19:213–28. https://doi.org/10.1038/nrm.2017.125

15. Welsh JA, Goberdhan DC, O'Driscoll L, Théry C, Witwer KW. MISEV2023: An updated guide to EV research and applications. Journal of Extracellular Vesicles. John Wiley & Sons, Ltd; 2024;13:e12416. https://doi.org/10.1002/jev2.12416

16. Cheng L, Hill AF. Therapeutically harnessing extracellular vesicles. Nat Rev Drug Discov. Nature Publishing Group; 2022;21:379–99. https://doi.org/10.1038/s41573-022-00410-w

17. Witwer KW, Wolfram J. Extracellular vesicles versus synthetic nanoparticles for drug delivery. Nat Rev Mater. Nature Publishing Group; 2021;6:103–6. https://doi.org/10.1038/s41578-020-00277-6

18. Deng D, Li X, Zhang J-J, Yin Y, Tian Y, Gan D, et al. Biotin–Avidin System-Based Delivery Enhances the Therapeutic Performance of MSC-Derived Exosomes. ACS Nano. American Chemical Society; 2023;17:8530–50. https://doi.org/10.1021/acsnano.3c00839

19. Gupta D, Zickler AM, El Andaloussi S. Dosing extracellular vesicles. Advanced Drug Delivery Reviews. 2021;178:113961. https://doi.org/10.1016/j.addr.2021.113961

20. Vader P, Mol EA, Pasterkamp G, Schiffelers RM. Extracellular vesicles for drug delivery. Advanced Drug Delivery Reviews. 2016;106:148–56. https://doi.org/10.1016/j.addr.2016.02.006

21. Gan J, Sun L, Chen G, Ma W, Zhao Y, Sun L. Mesenchymal Stem Cell Exosomes Encapsulated Oral Microcapsules for Acute Colitis Treatment. 2022;

22. Deng C, Hu Y, Conceição M, Wood MJA, Zhong H, Wang Y, et al. Oral delivery of layer-by-layer coated exosomes for colitis therapy. Journal of Controlled Release. 2023;354:635–50. https://doi.org/10.1016/j.jconrel.2023.01.017

23. Lee Y, Yoo C, Kim K-M, Kim S, Oh YK, Cho S, et al. Immunoregulatory protein-hybrid extracellular vesicles via self-loadable backbone cyclization for oral inflammatory bowel disease therapy. Bioactive Materials. 2026;58:70–88. https://doi.org/10.1016/j.bioactmat.2025.11.036

24. Schulz-Siegmund M, Aigner A. Nucleic acid delivery with extracellular vesicles.

Advanced Drug Delivery Reviews. 2021;173:89–111. https://doi.org/10.1016/j.addr.2021.03.005

25. Min DK, Kim YE, Kim MK, Choi SW, Park N, Kim J. Orally Administrated Inflamed Colon-Targeted Nanotherapeutics for Inflammatory Bowel Disease Treatment by Oxidative Stress Level Modulation in Colitis. ACS Nano. American Chemical Society; 2023;17:24404–16. https://doi.org/10.1021/acsnano.3c11089

26. Zhang X, Yuan Z, Wu J, He Y, Lu G, Zhang D, et al. An Orally-Administered Nanotherapeutics with Carbon Monoxide Supplying for Inflammatory Bowel Disease Therapy by Scavenging Oxidative Stress and Restoring Gut Immune Homeostasis. ACS Nano. American Chemical Society; 2023;17:21116–33. https://doi.org/10.1021/acsnano.3c04819

27. Zhou J, Li M, Chen Q, Li X, Chen L, Dong Z, et al. Programmable probiotics modulate inflammation and gut microbiota for inflammatory bowel disease treatment after effective oral delivery. Nat Commun. Nature Publishing Group; 2022;13:3432. https://doi.org/10.1038/s41467-022-31171-0

28. Vong LB, Mo J, Abrahamsson B, Nagasaki Y. Specific accumulation of orally administered redox nanotherapeutics in the inflamed colon reducing inflammation with dose–response efficacy. Journal of Controlled Release. 2015;210:19–25. https://doi.org/10.1016/j.jconrel.2015.05.275

29. Gibson GR, Hutkins R, Sanders ME, Prescott SL, Reimer RA, Salminen SJ, et al. Expert consensus document: The International Scientific Association for Probiotics and Prebiotics (ISAPP) consensus statement on the definition and scope of prebiotics. Nat Rev Gastroenterol Hepatol. Nature Publishing Group; 2017;14:491–502. https://doi.org/10.1038/nrgastro.2017.75

30. Le Bastard Q, Chapelet G, Javaudin F, Lepelletier D, Batard E, Montassier E. The effects of inulin on gut microbial composition: a systematic review of evidence from human studies. Eur J Clin Microbiol Infect Dis. 2020;39:403–13. https://doi.org/10.1007/s10096-019-03721-w

31. Hu Y, Zhu P, Deng J, Yu Y, Chen Q, Wu H, et al. Hydrogen Therapy and Lipopolysaccharide Trapping with MgB2@Inulin Gel for Reversing Colitis and Its Associated Psychiatric Complications via the Gut–Brain Axis. ACS Nano. American Chemical Society; 2025;19:27229–45. https://doi.org/10.1021/acsnano.5c03843

32. Wu S, Hu Y, Tao Z, Yu Y, Zhu P, Li T, et al. Comprehensive Management of Ulcerative Colitis and its Associated Intra-Extra Intestinal Complications with a Multifunctional Inulin Hydrogel Complex. [cited 2026 June 26]; https://doi.org/10.1002/smll.202500726

33. Fan Q, Kan C, Wang K, Zhu H, Zhang Y, Lu M, et al. Oral colon targeted curcumin-based nanocomposite inulin hydrogel for alleviating intestinal inflammation and dysbiosis. J Nanobiotechnol. 2026;24:408. https://doi.org/10.1186/s12951-026-04318-0

34. Ejima H, Richardson JJ, Liang K, Best JP, van Koeverden MP, Such GK, et al. One-Step Assembly of Coordination Complexes for Versatile Film and Particle Engineering. Science. American Association for the Advancement of Science; 2013;341:154–7. https://doi.org/10.1126/science.1237265

35. Lin Z, Liu H, Richardson JJ, Xu W, Chen J, Zhou J, et al. Metal–phenolic network composites: from fundamentals to applications. Chem Soc Rev. 2024;53:10800–26. https://doi.org/10.1039/d3cs00273j

36. Buschmann D, Mussack V, Byrd JB. Separation, characterization, and standardization of extracellular vesicles for drug delivery applications. Advanced Drug Delivery Reviews. 2021;174:348–68. https://doi.org/10.1016/j.addr.2021.04.027

37. Guo J, Ping Y, Ejima H, Alt K, Meissner M, Richardson JJ, et al. Engineering Multifunctional Capsules through the Assembly of Metal–Phenolic Networks. Angewandte Chemie International Edition. 2014;53:5546–51. https://doi.org/10.1002/anie.201311136

38. Richter M, Vader P, Fuhrmann G. Approaches to surface engineering of extracellular vesicles. Advanced Drug Delivery Reviews. 2021;173:416–26. https://doi.org/10.1016/j.addr.2021.03.020

39. Nguyen J, Fuhrmann G. Extracellular Vesicles - A Versatile Biomaterial. Adv Healthc Mater. 2022;11:e2200192. https://doi.org/10.1002/adhm.202200192

40. van Niel G, Carter DRF, Clayton A, Lambert DW, Raposo G, Vader P. Challenges and directions in studying cell–cell communication by extracellular vesicles. Nat Rev Mol Cell Biol. Nature Publishing Group; 2022;23:369–82. https://doi.org/10.1038/s41580-022-00460-3

41. Han C, Sheng Y, Wang J, Zhou X, Li W, Zhang C, et al. NOX4 promotes mucosal barrier injury in inflammatory bowel disease by mediating macrophages M1 polarization through ROS. International Immunopharmacology. 2022;104:108361. https://doi.org/10.1016/j.intimp.2021.108361

42. Tao S, Song M, Fan J, Zhu F, Lv T, Wei H. *Lactobacillus johnsonii*-derived extracellular vesicles carrying GAPDH protect against ulcerative colitis through modulating macrophage polarization. Journal of Advanced Research. 2026;81:409–24. https://doi.org/10.1016/j.jare.2025.06.035

43. Zhang X, Yang H, He Y, Zhang D, Lu G, Ren M, et al. Yeast-Inspired Orally-Administered Nanocomposite Scavenges Oxidative Stress and Restores Gut Immune Homeostasis for Inflammatory Bowel Disease Treatment. ACS Nano. American Chemical Society; 2025;19:7350–69. https://doi.org/10.1021/acsnano.4c18099

44. Zhang X, Zhao X, Hua Z, Xing S, Li J, Fei S, et al. ROS-triggered self-disintegrating and pH-responsive astaxanthin nanoparticles for regulating the intestinal barrier and colitis. Biomaterials. 2023;292:121937. https://doi.org/10.1016/j.biomaterials.2022.121937

45. Fraschilla I, Amatullah H, Rahman R-U, Jeffrey KL. Immune chromatin reader SP140 regulates microbiota and risk for inflammatory bowel disease. Cell Host & Microbe. 2022;30:1370-1381.e5. https://doi.org/10.1016/j.chom.2022.08.018

46. Rooks MG, Garrett WS. Gut microbiota, metabolites and host immunity. Nat Rev Immunol. Nature Publishing Group; 2016;16:341–52. https://doi.org/10.1038/nri.2016.42

47. Cao F, Jin L, Gao Y, Ding Y, Wen H, Qian Z, et al. Artificial-enzymes-armed Bifidobacterium longum probiotics for alleviating intestinal inflammation and microbiota dysbiosis. Nat Nanotechnol. Nature Publishing Group; 2023;18:617–27. https://doi.org/10.1038/s41565-023-01346-x

48. Abdulqadir R, Engers J, Al-Sadi R. Role of *Bifidobacterium* in Modulating the Intestinal Epithelial Tight Junction Barrier: Current Knowledge and Perspectives. Current Developments in Nutrition. 2023;7:102026. https://doi.org/10.1016/j.cdnut.2023.102026

49. Furusawa Y, Obata Y, Fukuda S, Endo TA, Nakato G, Takahashi D, et al. Commensal microbe-derived butyrate induces the differentiation of colonic regulatory T cells. Nature. Nature Publishing Group; 2013;504:446–50. https://doi.org/10.1038/nature12721

50. Arpaia N, Campbell C, Fan X, Dikiy S, van der Veeken J, deRoos P, et al. Metabolites produced by commensal bacteria promote peripheral regulatory T-cell generation. Nature. Nature Publishing Group; 2013;504:451–5. https://doi.org/10.1038/nature12726

51. Agus A, Planchais J, Sokol H. Gut Microbiota Regulation of Tryptophan Metabolism in Health and Disease. Cell Host & Microbe. 2018;23:716–24. https://doi.org/10.1016/j.chom.2018.05.003

52. Ogilvie LA, Jones BV. Dysbiosis modulates capacity for bile acid modification in the gut microbiomes of patients with inflammatory bowel disease: a mechanism and marker of disease? Gut. 2012;61:1642–3. https://doi.org/10.1136/gutjnl-2012-302137

53. Donowitz M. Arachidonic acid metabolites and their role in inflammatory bowel disease: An update requiring addition of a pathway. Gastroenterology. 1985;88:580–7. https://doi.org/10.1016/0016-5085(85)90525-6

54. Zelante T, Iannitti RG, Cunha C, De Luca A, Giovannini G, Pieraccini G, et al. Tryptophan Catabolites from Microbiota Engage Aryl Hydrocarbon Receptor and Balance Mucosal Reactivity via Interleukin-22. Immunity. 2013;39:372–85. https://doi.org/10.1016/j.immuni.2013.08.003

55. Aust A-C, Benesova E, Vidova V, Coufalikova K, Smetanova S, Borek I, et al. Profiling Tryptophan Catabolites of Human Gut Microbiota and Acute-Phase Protein Levels in Neonatal Dried Blood Specimens. Front Microbiol. 2021;12:665743. https://doi.org/10.3389/fmicb.2021.665743

56. Hang S, Paik D, Yao L, Kim E, Trinath J, Lu J, et al. Bile acid metabolites control TH17

and Treg cell differentiation. Nature. Nature Publishing Group; 2019;576:143–8. https://doi.org/10.1038/s41586-019-1785-z

57. Koh A, Molinaro A, Ståhlman M, Khan MT, Schmidt C, Mannerås-Holm L, et al. Microbially Produced Imidazole Propionate Impairs Insulin Signaling through mTORC1. Cell. 2018;175:947-961.e17. https://doi.org/10.1016/j.cell.2018.09.055

58. Wang L, Yang Y, Zhang Y, Shi J, Fan W, Yang H, et al. Reactive Oxygen Species-Activatable Topological Transition Nanogel Integrated with cfDNA Degradation Function for Adaptive Barrier Repair in Inflammatory Bowel Disease. ACS Nano. American Chemical Society; 2026;20:6666–84. https://doi.org/10.1021/acsnano.5c15244

59. Mills KHG. IL-17 and IL-17-producing cells in protection versus pathology. Nat Rev Immunol. Nature Publishing Group; 2023;23:38–54. https://doi.org/10.1038/s41577-022-00746-9

60. Hayden MS, Ghosh S. Shared Principles in NF-κB Signaling. Cell. 2008;132:344–62. https://doi.org/10.1016/j.cell.2008.01.020

61. Neurath MF. Cytokines in inflammatory bowel disease. Nat Rev Immunol. Nature Publishing Group; 2014;14:329–42. https://doi.org/10.1038/nri3661

62. Banerjee S, Biehl A, Gadina M, Hasni S, Schwartz DM. JAK–STAT Signaling as a Target for Inflammatory and Autoimmune Diseases: Current and Future Prospects. Drugs. 2017;77:521–46. https://doi.org/10.1007/s40265-017-0701-9

63. Cho JH. The genetics and immunopathogenesis of inflammatory bowel disease. Nat Rev Immunol. Nature Publishing Group; 2008;8:458–66. https://doi.org/10.1038/nri2340

Supplementary Files

This is a list of supplementary files associated with this preprint. Click to download.

- 4Supportinginformation.docx
- 17.tif
- 18.tif
- 15.tif
- 4.tif
- 12.tif
- 16.tif
- 5.tif
- 13.tif
- 1.tif
- 22.tif
- 21.tif
- 14.tif
- 6.tif
- 2.tif
- 19.tif
- 3.tif
- 7.tif
- 9.tif
- 10.tif
- 8.tif
- 11.tif
- 20.tif